

HERSCHEL/PACS SURVEY OF PROTOPLANETARY DISKS IN TAURUS/AURIGA—OBSERVATIONS OF [O I] AND [C II], AND FAR-INFRARED CONTINUUM

CHRISTIAN D. HOWARD^{1,2}, GÖRAN SANDELL¹, WILLIAM D. VACCA¹, GASPARD DUCHÊNE^{3,4}, GEOFFREY MATHEWS^{5,6}, JEAN-CHARLES AUGEREAU⁴, DAVID BARRADO^{7,8}, WILLIAM R. F. DENT⁹, CARLOS EIROA¹⁰, CAROL GRADY^{11,12,13}, INGA KAMP¹⁴, GWENDOLYN MEEUS¹⁰, FRANCOIS MÉNARD^{4,15}, CHRISTOPHE PINTÉ⁴, LINDA PODIO⁴, PABLO RIVIERE-MARICHALAR⁷, AKI ROBERGE¹¹, WING-FAI THI⁴, SILVIA VICENTE¹⁴, AND JONATHAN P. WILLIAMS⁶

¹ SOFIA-USRA, NASA Ames Research Center, MS 232-12, Building N232, Rm. 146, P.O. Box 1, Moffett Field, CA 94035-0001, USA

² Google, 1600 Amphitheatre Parkway, Mountain View, CA 94043, USA

³ Astronomy Department, University of California, Berkeley, CA 94720-3411, USA

⁴ UJF-Grenoble 1/CNRS-INSU, Institut de Planétologie et d'Astrophysique (IPAG) UMR 5274, F-38041 Grenoble, France

⁵ Leiden Observatory, Leiden University, P.O. Box 9513, 2300 RA Leiden, The Netherlands

⁶ Institute for Astronomy (IfA), University of Hawaii, 2680 Woodlawn Drive, Honolulu, HI 96822, USA

⁷ Centro de Astrobiología, Depto. Astrofísica (CSIC/INTA), ESAC Campus, P.O. Box 78, E-28691 Villanueva de la Cañada, Spain

⁸ Calar Alto Observatory, Centro Astronómico Hispano Alemán, C/Jesús Durbán Remón, E-04004 Almería, Spain

⁹ ALMA SCO, Alonso de Córdova 3107, Vitacura, Santiago, Chile

¹⁰ Dep. de Física Teórica, Fac. de Ciencias, UAM Campus Cantoblanco, E-28049 Madrid, Spain

¹¹ Exoplanets & Stellar Astrophysics Laboratory, NASA Goddard Space Flight Center, Code 667, Greenbelt, MD 20771, USA

¹² Eureka Scientific, 2452 Delmer, Suite 100, Oakland, CA 96002, USA

¹³ Goddard Center for Astrobiology, NASA Goddard Space Flight Center, Greenbelt, MD 20771, USA

¹⁴ Kapteyn Astronomical Institute, Postbus 800, 9700 AV Groningen, The Netherlands

¹⁵ UMI-FCA (UMI 3386: CNRS France, and U de Chile/PUC/U Concepcion), Santiago, Chile

Received 2013 March 8; accepted 2013 August 19; published 2013 September 20

ABSTRACT

The *Herschel Space Observatory* was used to observe ~ 120 pre-main-sequence stars in Taurus as part of the GASPS Open Time Key project. Photodetector Array Camera and Spectrometer was used to measure the continuum as well as several gas tracers such as [O I] 63 μm , [O I] 145 μm , [C II] 158 μm , OH, H₂O, and CO. The strongest line seen is [O I] at 63 μm . We find a clear correlation between the strength of the [O I] 63 μm line and the 63 μm continuum for disk sources. In outflow sources, the line emission can be up to 20 times stronger than in disk sources, suggesting that the line emission is dominated by the outflow. The tight correlation seen for disk sources suggests that the emission arises from the inner disk (< 50 AU) and lower surface layers of the disk where the gas and dust are coupled. The [O I] 63 μm is fainter in transitional stars than in normal Class II disks. Simple spectral energy distribution models indicate that the dust responsible for the continuum emission is colder in these disks, leading to weaker line emission. [C II] 158 μm emission is only detected in strong outflow sources. The observed line ratios of [O I] 63 μm to [O I] 145 μm are in the regime where we are insensitive to the gas-to-dust ratio, neither can we discriminate between shock or photodissociation region emission. We detect no Class III object in [O I] 63 μm and only three in continuum, at least one of which is a candidate debris disk.

Key words: circumstellar matter – planetary systems – protoplanetary disks – stars: pre-main sequence

Online-only material: color figures

1. INTRODUCTION

Low-mass stars are born with protoplanetary disks, canonically composed of 1% dust by mass (adopted from the interstellar medium gas/dust mass ratio), the remaining portion in gas. For low-mass stars the gas has largely disappeared on timescales of 6–7 Myr (Haisch et al. 2001; Hernández et al. 2008). Understanding the early evolution of stars requires the understanding of their accompanying protoplanetary disks of gas and dust.

Gas in Protoplanetary Systems (GASPS) is a large Open Time Key Project on the *Herschel Space Observatory* (Pilbratt et al. 2010) studying the evolution of gas in protoplanetary disks. In total the project surveyed ~ 250 nearby (≤ 200 pc) low- and intermediate-mass stars (0.3–8 M_{\odot}), from young (0.5 Myr) stars with massive disks to older (30 Myr) stars with very little dust excess. For this study we are using the Photodetector Array Camera and Spectrometer (PACS; Poglitsch et al. 2010) to observe the fine-structure lines of [C II] at 158 μm and [O I] at 63.2 and 145 μm as well as several H₂O, OH, and high rotational transitions of CO tracing mainly hot gas. We also

use the PACS imager to measure broadband continuum fluxes for a large portion of the sample. The goal is to understand the transition from gas rich protoplanetary disks to gas poor debris disks, and the timescales on which the gas dissipates. For a more detailed description of GASPS, see Dent et al. (2013).

The largest sample of GASPS sources are in the Taurus star forming region. As one of the closest star forming regions to the Sun (distance of ~ 140 pc), the Taurus group provides a unique opportunity to obtain a statistical sample of largely coeval protoplanetary disks encompassing a wide range of disk masses. The majority of GASPS sources in Taurus are class II objects (classical T Tauri stars, CTTs), with spectral types ranging from mid-F to early M, and with stellar masses of ~ 0.3 to 1.4 M_{\odot} , having dissipated their envelope of accreting material and leaving behind the protostar and a disk of gas and dust (see, e.g., Kenyon et al. 2008). Of all the gas probes used by GASPS, the [O I] 63 μm line is by far the most sensitive gas tracer, at least for protoplanetary disks (Pinté et al. 2010).

The [O I] 63 μm line is known to be strong in photodissociation regions (PDR; Tielens & Hollenbach 1985), and also

in shocks (Hollenbach & McKee 1989; Flower & Pineau des Fôrets 2010). Because of this, it is necessary to isolate the component of the emission arising from the disk itself from that arising from jets or outflows, which are common in young T Tauri stars. The velocity resolution of PACS is insufficient to separate the low velocity disk emission from the outflow emission and for most objects the outflow is spatially unresolved in [O I] $63\ \mu\text{m}$. Podio et al. (2012) have spatially resolved the [O I] $63\ \mu\text{m}$ emission in a few of the strongest jet sources in the Taurus sample. In our analysis we therefore distinguish between sources that are already known to have jets/outflows based on previous observations and sources which have very weak or undetectable outflows; in the latter the [O I] emission, if detected, is expected to be dominated by emission from the protoplanetary disk. The relative importance of FUV and X-ray irradiation for the [O I] line emission from the Taurus disk sources is explored in a forthcoming paper by Aresu et al. (2013). Detailed SED modeling and molecular emission lines will be discussed in a future paper.

In Section 2 we discuss the Taurus sample, In Section 3 we discuss the observations and reduction for both spectroscopy and photometry as well as pointing issues that arose in some observations. Section 4 discusses the results for the [O I] and [C II] fine structure lines, followed with a discussion of what we learned in Section 5. Section 5.6 gives a brief summary of our results for Class III objects and in Section 5.7 we comment on a few individual objects. Section 6 gives the summary and conclusions of this study.

2. THE TAURUS–AURIGA DARK YOUNG STELLAR ASSOCIATION

The Taurus–Auriga cloud complex is one of the closest (140 pc; Bertout et al. 1999; Torres et al. 2009) active star forming regions, with a young stellar association containing at least 250 cluster members (Rebull et al. 2010, 2011). It does not have any O and B stars, but it has a rich population of pre-main-sequence (PMS) low-mass T Tauri stars and brown dwarfs. The Taurus–Auriga dark cloud complexes extend over $\sim 10^\circ$ of the sky with a depth of ~ 20 pc (Torres et al. 2009). The youngest stars, Class I protostars, are found toward the center of opaque dark clouds. Likewise the CTTs (Class II) are also concentrated toward dark clouds, whereas the Class III objects, weak-lined T Tauri stars, are more widely distributed over the whole region. Our Taurus sample also includes nine confirmed or suspected transitional disk objects. Transitional disks, which were first discovered by Strom et al. (1989), are believed to be transition objects between CTTs and weak-lined T Tauri stars. They have large mid- to far-infrared excesses, but weak (pre-transitional disks) or no excess in the near-infrared (Najita et al. 2007; Espaillat et al. 2011). Both pre-transitional and transitional disks have large gaps or cavities largely void of gas and dust in the inner disk, which in several cases have been resolved with millimeter interferometry (Piétu et al. 2006; Dutrey et al. 2008; Brown et al. 2009; Andrews et al. 2011). The majority of the PMS population in Taurus has an age of 1–3 Myr, although there is certainly an age spread. Some stars are as young as 0.5 Myr and there are a few objects as old as 15–20 Myr (Hartmann 2003; Küçük & Akkaya 2010).

Some of the younger, more deeply embedded T Tauri stars drive Herbig–Haro (HH) flows or well-collimated jets, typically seen in the optical [O I], $H\alpha$, [N II] $\lambda\lambda 6548, 6583$, and [S II] $\lambda\lambda 6717, 6731$ emission lines (Mundt & Fried 1983; Gómez et al. 1997). Since we try to discriminate between disk emission

and outflow emission in our GASPS observations, it is therefore important to identify which stars power optical jets or HH flows. For this we have mainly used the tabulation provided by Kenyon et al. (2008), but we have also identified a few additional ones: AA Tau, DL Tau, and V773 Tau, see Section 5.7, IRAS 04385+2805 (Glauser et al. 2008), and SU Aur (Chakraborty & Ge 2004). Stars that we define as jet/outflow sources must have a jet imaged in $H\alpha$, [O I] $\lambda 6300$, [S II] $\lambda 6371$ or be associated with HH objects, show a high velocity molecular outflow, or a broad ($> 50\ \text{km s}^{-1}$), typically blue-shifted, emission line profiles in [O I] $\lambda 6300$ (see, e.g., Hartigan et al. 1995).

For the most part, our analysis leaves aside the issue of multiplicity. About half of our targets are known binary or higher-order multiple systems, with separation ranging from $\lesssim 0.1$ AU to as much as 2000 AU. On an individual object basis, the interpretation of our observations can be severely affected by the possible presence of several circumstellar and/or circumbinary disks. However, as discussed in Section 5.5, it appears that the effect of multiplicity on both far-infrared continuum and line emission is relatively modest.

3. OBSERVATIONS AND DATA REDUCTION

The observations reported herein were carried out with *Herschel* from 2010 February through 2011 March. We obtained photometry and spectroscopy utilizing the PACS instrument aboard *Herschel*. For a description of PACS observing modes, see Poglitsch et al. (2010).

3.1. Photometry

All photometric observations of our targets in Taurus were made in “mini-scan” mode, i.e., by doing short, 3' scans with medium scan speed of $20''\ \text{s}^{-1}$, and with 10 4'' steps in the direction orthogonal to the scan. Executing such an observation takes 276 s. Two bands, either blue and red, or green and red, are recorded simultaneously. The blue filter is centered on $70\ \mu\text{m}$, the green filter is centered at $100\ \mu\text{m}$ and the red at $160\ \mu\text{m}$ (see, e.g., Poglitsch et al. 2010). All targets have been observed in the $70\ \mu\text{m}$ and the $160\ \mu\text{m}$ bands and many were also observed in the $100\ \mu\text{m}$ filter (see Table 1). Almost all the Taurus photometric observations were carried out in two scan directions (70° and 110°) providing a smoother background and hence more accurate photometry. However, some of the early photometry was done with only a single blue/red mini-scan. Only T Tauri is spatially resolved at $70\ \mu\text{m}$.¹⁶ An extended disk is, however, detected around HD 283759, an F5 star, but proper motion studies (Massarotti et al. 2005) show conclusively that the star is not a member of the Taurus association.

All the photometric data were originally reduced using the *Herschel* Interactive Processing Environment, HIPE¹⁷ v7.0, but we later re-reduced all detected sources in HIPE v9.0, where the reduction scripts provide iterative masked high pass filtering, resulting in better deglitching and smoother backgrounds, especially in the red. For the blue filter the results were essentially identical, i.e., within 1%–2%. The final images were imported to the STARLINK program Gaia for photometry and further analysis. For strong sources we performed aperture

¹⁶ The emission from UZ Tau is also extended, but here the emission originates from two binaries UZ Tau E and UZ Tau W, which are separated by 3'6 and which both are surrounded by disks, see, e.g., Harris et al. (2012).

¹⁷ HIPE is a joint development by the *Herschel* Science Ground Segment Consortium, consisting of ESA, the NASA *Herschel* Science Center, and the HIFI, PACS, and SPIRE consortia.

Table 1
GASPS Taurus Observations: PACS Photometry

Name	SED Class	70 μ m (Jy)	100 μ m (Jy)	160 μ m (Jy)	Comments
CIDA 2	III	<0.009	<0.009	<0.022	Empty field
CIDA 10	III	<0.008	...	<0.028	Empty field
CoKu Tau 2	I	1.30 \pm 0.20	1.32 \pm 0.20	1.53 \pm 0.30	34'' west of HL Tau
CoKu Tau 4 ^a	II	1.15 \pm 0.06	0.85 \pm 0.08	0.64 \pm 0.10	
CW Tau ^b	II	1.79 \pm 0.18	...	1.82 \pm 0.18	Same field as V773 Tau
CX Tau ^c	T	0.33 \pm 0.03	0.25 \pm 0.03	0.25 \pm 0.03	S1
CY Tau	II	0.22 \pm 0.01	0.29 \pm 0.03	0.35 \pm 0.04	S1
DG Tau	II	23.8 \pm 2.4	23.3 \pm 2.3	18.30 \pm 2.0	Cloud emission, S2
DG Tau B	I	15.4 \pm 1.5	18.0 \pm 1.8	18.10 \pm 2.0	Same field as DG Tau
DH Tau A	II	0.47 \pm 0.05	0.48 \pm 0.05	0.41 \pm 0.04	
DI Tau AB	III	<0.01	<0.01	<0.03	Near DH Tau
DK Tau A	II	1.17 \pm 0.12	1.07 \pm 0.11	0.83 \pm 0.08	
DL Tau	II	1.32 \pm 0.13	1.54 \pm 0.15	1.93 \pm 0.19	S1
DM Tau	T	0.78 \pm 0.08	0.85 \pm 0.08	0.78 \pm 0.08	
DO Tau ^d	II	5.1 \pm 0.80	4.7 \pm 0.70	4.1 \pm 0.70	
DP Tau	II	0.67 \pm 0.07	0.36 \pm 0.04	0.20 \pm 0.03	Cloud emission
DQ Tau ^e	II	1.37 \pm 0.10	1.28 \pm 0.12	1.02 \pm 0.10	S1, field includes Haro 6-37
DS Tau	II	0.22 \pm 0.02	0.33 \pm 0.03	0.26 \pm 0.03	
FF Tau AB	III	<0.009	<0.010	<0.028	S2
FM Tau ^b	II	0.47 \pm 0.07	...	0.24 \pm 0.03	
FO Tau AB	T	0.51 \pm 0.05	0.39 \pm 0.04	0.21 \pm 0.03	S1
FP Tau ^c	II	0.33 \pm 0.03	0.34 \pm 0.06	0.38 \pm 0.04	S1
FT Tau	II	0.73 \pm 0.07	0.95 \pm 0.09	1.27 \pm 0.19	
FW Tau ABC	III	0.030 \pm 0.004	0.033 \pm 0.004	0.070 \pm 0.040	S1, cloud emission
FX Tau A	II	0.39 \pm 0.04	0.36 \pm 0.04	0.22 \pm 0.03	
GG Tau Aab	II	4.22 \pm 0.42	6.56 \pm 0.66	8.41 \pm 0.84	Extended
GG Tau Bab	II	0.21 \pm 0.02	
GH Tau AB	II	0.37 \pm 0.04	0.52 \pm 0.05	0.27 \pm 0.03	S1, field includes V807 Tau
GI Tau ^f	II	0.67 \pm 0.07	0.50 \pm 0.05	0.33 \pm 0.06	
GK Tau ^f	II	0.90 \pm 0.09	0.59 \pm 0.06	0.35 \pm 0.06	
Haro 6-37 B ^e	II	0.96 \pm 0.10	0.90 \pm 0.09	1.25 \pm 0.12	
HBC 347	III	<0.009	<0.009	<0.019	S2
HBC 352/353	III	<0.007	...	<0.017	S1
HBC 354/355	III	<0.007	...	<0.022	Empty field
HBC 356/357	III	<0.010	<0.011	<0.023	S1
HBC 358/359	III	<0.007	...	<0.020	S2
HBC 360/361	III	<0.009	<0.010	<0.020	Empty field
HBC 362	III	<0.008	...	<0.019	S4
HBC 372	III	<0.009	<0.009	<0.021	Empty field
HBC 376	III	<0.009	<0.009	<0.016	S3
HBC 388	III	<0.007	...	<0.018	Empty field
HBC 392	III	<0.007	...	<0.013	Empty field
HBC 407	III	<0.009	<0.009	<0.017	Empty field
HBC 412 AB	III	<0.009	<0.009	<0.018	Empty field
HD 283572	III	<0.008	<0.009	<0.027	S1
HD 283759 ^g	S	0.52 \pm 0.05	0.69 \pm 0.07	0.57 \pm 0.06	S1
HL Tau	I	75.3 \pm 7.5	72.3 \pm 7.2	54.7 \pm 8.2	Cloud emission, 4 T Tauri stars, S1
HN Tau A	II	1.02 \pm 0.10	...	0.61 \pm 0.06	S4
HO Tau	II	0.10 \pm 0.01	0.11 \pm 0.01	0.14 \pm 0.02	S2
HV Tau C ^d	I?	1.55 \pm 0.16	1.68 \pm 0.18	1.45 \pm 0.24	
IQ Tau	II	0.74 \pm 0.07	0.78 \pm 0.08	0.81 \pm 0.08	S2
IW Tau	III	<0.009	<0.010	<0.030	S1
J04305171+2441475	II	2.85 \pm 0.29	3.11 \pm 0.31	3.06 \pm 0.31	Cloud emission, 35'' north of ZZ Tau
J1-4872	III	<0.009	<0.009	<0.027	S3
J1-507	III	<0.008	<0.008	<0.021	Empty field
J1-665	III	<0.009	<0.009	<0.025	Empty field
J2-2041	III	<0.008	<0.009	<0.013	S1
JH 108	III	<0.008	<0.009	<0.021	S2
JH 223	II	0.114 \pm 0.011	0.109 \pm 0.011	0.076 \pm 0.016	
JH 56	II	0.027 \pm 0.003	0.017 \pm 0.003	<0.04	Cloud emission
L 1551-51	III	<0.009	<0.009	<0.016	Empty field
L 1551-55	III	<0.009	<0.009	<0.016	Empty field
LkCa 1	III	<0.009	<0.009	<0.021	Empty field
LkCa 3	III	<0.009	<0.009	<0.017	S1
LkCa 4	III	<0.009	<0.009	<0.034	Empty field

Table 1
(Continued)

Name	SED Class	70 μm (Jy)	100 μm (Jy)	160 μm (Jy)	Comments
LkCa 5	III	<0.009	<0.009	<0.029	S1, cloud emission
LkCa 14	III	<0.009	<0.009	<0.028	S2
LkCa 15	T	1.23 \pm 0.12	1.48 \pm 0.15	1.78 \pm 0.18	
LkCa 19	III	<0.009	<0.009	<0.015	
LkCa 21	III	<0.012	...	<0.051	In same field as RY Tau
RW Aur A	II	2.47 \pm 0.15	2.94 \pm 0.29	1.74 \pm 0.17	S2
RY Tau	T?	14.13 \pm 1.40	...	8.81 \pm 0.88	Cloud emission
SAO 76411	III	<0.012	<0.011	<0.020 mJy S1	
SAO 76428	III	<0.009	<0.009	<0.020 mJy S2	
StHA 34 ^h	II	0.053 \pm 0.006	0.039 \pm 0.005	0.025 \pm 0.025	S2
Tau L1495 14	I	1.11 \pm 0.22	...	1.45 \pm 0.29	In same field as V773 Tau, edge of field
T Tau NS ⁱ	II/I	170 \pm 20	143 \pm 21	100 \pm 20	Extended, cloud emission
UZ Tau Eab+Wab	II	2.03 \pm 0.20	2.13 \pm 0.21	2.04 \pm 0.20	
V397 Aur	III	0.016 \pm 0.003	...	0.016 \pm 0.007	
V773 Tau ^b	II	0.81 \pm 0.08	...	0.25 \pm 0.03	
V807 Tau AB	II	0.51 \pm 0.05	0.72 \pm 0.07	0.35 \pm 0.04	S2, field includes GH Tau
V819 Tau	II/III	0.030 \pm 0.003	0.017 \pm 0.003	<0.050	S1, faint cloud emission
V826 Tau AB	III	<0.009	<0.009	<0.017	Empty field
V827 Tau	III	<0.009	<0.009	<0.018	Empty field
V830 Tau	III	<0.009	<0.010	<0.030	Cloud emission
V836 Tau	T	0.21 \pm 0.02	0.30 \pm 0.03	0.27 \pm 0.05	S1
V927 Tau	III	<0.009	<0.009	<0.032	Empty field
V928 Tau	III	<0.009	<0.011	<0.053	Cloud emission
V1096 Tau	III	<0.009	<0.010	<0.030	Cloud emission.
V1213 Tau	I	0.41 \pm 0.04	0.51 \pm 0.05	0.59 \pm 0.012	In same field as HL Tau
VY Tau AB	II	0.30 \pm 0.03	0.29 \pm 0.03	0.22 \pm 0.02	S2
Wa Tau I	III	<0.009	<0.009	<0.014	S2
XZ Tau AB	II	5.77 \pm 0.87	4.71 \pm 0.71	4.13 \pm 0.80	23" east of HL Tau
ZZ Tau	II	0.052 \pm 0.005	0.051 \pm 0.005	0.025 \pm 0.02	

Notes. Upper limits are 3σ . The commonly used source notations CIDA NN and J1-NN are not known to SIMBAD, which instead uses [BCG93] NN and [HJS91] NN, respectively. In the comment field Sn ($n = 1, 2, 3$ etc.) lists the number of “background” sources we find in each field.

^a Star surrounded by extended nebulosity, see text.

^b V773 Tau, FM Tau, CW Tau and Tau L1495 14 in the same field.

^c CX Tau and FP Tau in the same field.

^d DO Tau and HV Tau in the same field. Cloud emission, see text.

^e Haro 6-37 and DQ Tau in the same field.

^f GI Tau and GK Tau in the same field; some nebulosity to the east in red.

^g Emission is extended! Not a member of the Taurus association (Massarotti et al. 2005).

^h Stronger source within 18" to the NW.

ⁱ Extended.

photometry with a 12" aperture, while we used 6"–9" apertures for faint sources and applied the aperture corrections determined by the PACS team (Müller et al. 2011). An annulus extending from 60"–70" was used for estimating the sky background. In some cases, where stars were near the edge of the image, where we had multiple stars, or where there was extended background emission in the image, the sky emission was estimated from the average of several, “clean” areas in the image. For the 70 μm and 100 μm bands the background is very close to zero. In a few cases the star was surrounded by emission from the surrounding cloud. This emission is mostly seen at 160 μm , but can be visible in the 100 μm band. In these cases we used a 6"–8" aperture, with the appropriate aperture correction applied. The point source calibration for the PACS images has an absolute accuracy of 3% in the 70 μm and 100 μm band and better than 5% at 160 μm (Müller et al. 2011). In our analysis we do not reach such accuracy. Many of our target stars are embedded in or are in the direction of dark clouds, and variations in the background limits the photometric accuracy. We therefore

estimate our photometric accuracy to be about 10%. In the 70 μm and 100 μm bands the 3σ upper limits are typically about 9 mJy. In the 160 μm band the noise is much higher due to the presence of “cirrus”-like emission from dust clouds. Typical 3σ upper limits are about 20 mJy. All flux densities are given in Table 1 as measured, i.e., without color corrections. The color corrections, however, are small (<2%) for all our targets and do not affect our analysis. We also list the SED classes in Tables 1 and 2. The SED classification comes primarily from Luhman et al. (2010) and or Rebull et al. (2010); if they differ we list both. Some weak-line T Tauri star (WTTS) were not observed by Luhman et al. or Rebull et al. If we found no indication for an infrared excess we assigned them as Class III. Transitional disks are labeled T.

Some fields also show faint unrelated sources. Almost all of them are extragalactic background sources. A few, however, do coincide with faint 2MASS and WISE sources, and could be low-mass T Tauri stars. We therefore also list the number of “background” sources we find in each field in Table 1.

Table 2
PACS [O I] 63, [O I] 145, and [C II] 158 Flux Densities and Other Possible Detections

Name	Jet/ Outflow	SED Class	[O I] 63 (10^{-16} W m $^{-2}$)	[O I] 145 (10^{-16} W m $^{-2}$)	[C II] 158 (10^{-16} W m $^{-2}$)	Other Lines
AA Tau	Y	II	0.22 ± 0.02	0.02 ± 0.01 (<0.02)	<0.02	1, 2, 4, 5, 9
BP Tau	N	II	0.10 ± 0.03	1
CI Tau	N	II	0.33 ± 0.05	0.02 ± 0.02 (<0.07)	<0.07	9
CIDA 2	N	III	<0.08	
CoKu Tau/4	N	II	0.22 ± 0.02	
CW Tau	Y	II	0.72 ± 0.04	0.05 ± 0.02	0.05 ± 0.01 (<0.05)	9
CX Tau	N	T	0.07 ± 0.03 (<0.08)	
CY Tau	N	II	0.12 ± 0.04	
DE Tau	N	II	0.07 ± 0.06 (<0.12)	0.04 ± 0.02	<0.04	9
DF Tau	Y	II	0.61 ± 0.06	0.06 ± 0.04 (<0.09)	0.05 ± 0.02 (<0.06)	
DG Tau	Y	II	13.40 ± 0.17	0.84 ± 0.05	1.87 ± 0.04	4, 5, 7, 8, 9
DG Tau B	Y	I	4.26 ± 0.12	0.27 ± 0.03	0.13 ± 0.02	9
DH Tau	N	II	0.07 ± 0.02 (<0.10)	
DI Tau	N	III	<0.14	
DK Tau	N	II	0.16 ± 0.03	<0.10	<0.15	
DL Tau	Y	II	0.22 ± 0.02	<0.14	<0.09	1
DM Tau	N	T	0.07 ± 0.02	<0.06	<0.06	1
DN Tau	N	T	0.06 ± 0.02	<0.06	0.05 ± 0.02 (<0.09)	
DO Tau	Y	II	0.71 ± 0.10	0.08 ± 0.01	0.03 ± 0.01 (<0.03)	2, 9
DP Tau	Y	II	1.48 ± 0.13	0.07 ± 0.02	0.12 ± 0.02	5, 9
DQ Tau	N	II	0.21 ± 0.04	<0.04	0.03 ± 0.01 (<0.04)	
DS Tau	N	II	0.09 ± 0.02	
FF Tau	N	III	<0.10	
FM Tau	N	II	0.10 ± 0.02 (<0.13)	<0.06	<0.06	
FO Tau	N	T	0.12 ± 0.05 (<0.12)	<0.05	<0.04	
FQ Tau	N	II	<0.09	<0.03	<0.06	
FS Tau A	Y	II/Flat	3.58 ± 0.05	0.18 ± 0.01	0.16 ± 0.01	1, 4, 5, 7, 8, 9, 10, 11
FT Tau	N	II	0.17 ± 0.05	
FW Tau	N	III	0.04 ± 0.02 (<0.08)	
FX Tau	N	II	<0.14	
GG Tau Aab	N	II	0.51 ± 0.04	0.03 ± 0.01 (<0.05)	<0.04	4, 5, 9
GH Tau	N	II	0.08 ± 0.04 (<0.16)	<0.03	<0.02	
GI/GK Tau ^a	N/Y	II	0.31 ± 0.14	
GM Aur	N	T	0.24 ± 0.05	<0.06	<0.10	
GO Tau	N	II	<0.06	
Haro 6-5B	Y	I	0.68 ± 0.11	0.04 ± 0.01 (<0.04)	0.06 ± 0.01	
Haro 6-13	Y	II	0.70 ± 0.05	0.03 ± 0.01 (<0.04)	<0.05	2, 4, 5, 9
Haro 6-37	N	II	0.10 ± 0.02	
HBC 347	N	III	<0.12	
HBC 356	N	III	<0.08	
HBC 358	N	III	<0.14	
HD 283572	N	III	<0.08	
HK Tau	N	II	0.34 ± 0.02	<0.04	<0.04	9
HL Tau	Y	I	5.13 ± 0.05	0.28 ± 0.02	0.36 ± 0.04	1, 2, 3, 4, 5, 7, 8, 9
HN Tau A	Y	II	0.41 ± 0.02	0.04 ± 0.01	<0.04	1
HO Tau	N	II	<0.10	
HV Tau C	Y	I?	0.52 ± 0.08	
IP Tau	N	T	0.06 ± 0.02 (<0.07)	
IQ Tau	N	II	0.15 ± 0.03	<0.11	<0.07	
IRAS 04158+2805	Y	I	0.57 ± 0.04	0.05 ± 0.02	<0.08	
IRAS 04385+2550	Y	II	0.49 ± 0.02	
J1-4827	N	III	<0.09	
LkCa 1	N	III	<0.08	
LkCa 3	N	III	<0.10	
LkCa 4	N	III	<0.10	
LkCa 5	N	III	<0.10	
LkCa 7	N	III	<0.09	
LkCa15	N	T	0.10 ± 0.02	<0.09	<0.11	
RW Aur	Y	II	1.54 ± 0.05	0.12 ± 0.03	<0.10	9, 10
RY Tau	Y	T?	1.05 ± 0.05	0.07 ± 0.02	<0.10	1, 2, 9
SU Aur	Y	II	0.86 ± 0.03	0.06 ± 0.02 (<0.06)	0.07 ± 0.02	9
T Tau	Y	II/I	81.80 ± 0.31	4.06 ± 0.04	2.29 ± 0.02	1, 2, 3, 4, 5, 6, 7, 8, 9, 10, 11
UX Tau A	N	T	0.34 ± 0.02	
UY Aur	Y	II	3.14 ± 0.04	0.17 ± 0.01	0.16 ± 0.01	1, 2, 4, 5, 7, 8, 9, 10

Table 2
(Continued)

Name	Jet/ Outflow	SED Class	[O I] 63 (10^{-16} W m $^{-2}$)	[O I] 145 (10^{-16} W m $^{-2}$)	[C II] 158 (10^{-16} W m $^{-2}$)	Other Lines
UZ Tau	Y	II	0.45 ± 0.14	<0.11	<0.07	
V710 Tau	N	II	0.10 ± 0.06 (<0.12)	
V773 Tau	Y	II	0.65 ± 0.03	1
V807 Tau	N	II	0.14 ± 0.05	<0.05	0.02 ± 0.01 (<0.04)	
V819 Tau	N	II/III	<0.09	
V836 Tau	N	T	0.05 ± 0.04 (<0.06)	
V927 Tau	N	III	<0.08	
V1096 Tau	N	III	<0.12	
VY Tau	N	II	<0.11	
XZ Tau	Y	II	3.61 ± 0.09	0.18 ± 0.04	0.24 ± 0.02	1, 2, 4, 5, 7, 8, 9
ZZ Tau	N	II	<0.10	

Notes. For sources where no line is detected, the 3σ upper limit is reported. Possible detections of other emission lines determined through visual inspection. The numbers refer to

- (1) o-H₂O 8₁₈ → 7₀₇
- (2) CH⁺ $J = 5 \rightarrow 4$
- (3) CO $J = 36 \rightarrow 35$
- (4) o-H₂O 4₂₃ → 3₁₂
- (5) OH 1/2-3/2 hfs
- (6) CO $J = 33 \rightarrow 32$
- (7) p-H₂O 3₂₂ → 2₁₁
- (8) CO $J = 29 \rightarrow 28$
- (9) CO $J = 18 \rightarrow 17$
- (10) o-H₂O 2₁₂ → 1₀₁
- (11) o-H₂O 2₂₁ → 2₁₂

^a Gi Tau and GK Tau are unresolved in spectroscopy.

Table 3
PACS Spectroscopy Settings

Obs. Mode	Setting	Grating Order	Camera	Observed Range (μ m)	Species	Transition	Wavelength (μ m)
LineSpec	A	3	Blue	62.68–63.68	[O I]	$^3P_1 \rightarrow ^3P_2$	63.184
		1	Red	188.77–190.30	o-H ₂ O	8 ₁₈ → 7 ₀₇	63.324
RangeSpec	B	2	Blue	72.00–73.05	CH ⁺	$J = 5 \rightarrow 4$	72.14
		1	Red	144–146.1	CO	$J = 36 \rightarrow 35$	72.843
	C	2	Blue	78.55–79.45	CO	$J = 18 \rightarrow 17$	144.784
		1	Red	157.1–158.9	[O I]	$^3P_0 \rightarrow ^3P_1$	145.525
D	2	2	Blue	89.45–90.50	o-H ₂ O	4 ₂₃ → 3 ₁₂	78.741
		1	Red	157.1–158.9	OH	$\frac{1}{2} \rightarrow \frac{3}{2}$ hfs	79.11/79.18
	1	2	Blue	89.45–90.50	CO	$J = 33 \rightarrow 32$	79.360
		1	Red	178.9–181.0	[C II]	$^2P_{3/2} \rightarrow ^2P_{1/2}$	157.741
E	2	2	Blue	89.45–90.50	p-H ₂ O	3 ₃₁ → 4 ₀₄	158.309
		1	Red	178.9–181.0	p-H ₂ O	3 ₂₂ → 2 ₁₁	89.988
	1	2	Blue	89.45–90.50	CH ⁺	$J = 4 \rightarrow 3$	90.02
		1	Red	178.9–181.0	CO	$J = 29 \rightarrow 28$	90.163
F	1	2	Blue	89.45–90.50	o-H ₂ O	2 ₁₂ → 1 ₀₁	179.527
		1	Red	178.9–181.0	CH ⁺	$J = 2 \rightarrow 1$	179.610
G	1	2	Blue	89.45–90.50	o-H ₂ O	2 ₂₁ → 2 ₁₂	180.488
		1	Red	178.9–181.0	o-H ₂ O	2 ₂₁ → 2 ₁₂	180.488

Note. The primary lines are highlighted in bold.

3.2. Spectroscopy

3.2.1. Observations

We observed the Taurus sample with PACS using both chopped line and range spectroscopy modes, targeting primarily [O I] 63 and 145 μ m and the [C II] 158 μ m lines, but also the CO, OH, H₂O, CH⁺, and DCO⁺ lines. Table 3 shows the setup for both line spectroscopy (henceforth linespec) and range spectroscopy (rangespec). The primary lines are highlighted

in bold. The effective spectral resolution is 0.020 μ m at [O I] 63 μ m (88 km s $^{-1}$) and 0.126 μ m for the [C II] 158 μ m line (239 km s $^{-1}$). Therefore the observed lines are unresolved in velocity even for the shortest wavelengths, which have the best spectral resolution, except in a few strong outflow sources, where the lines can be broad (Podio et al. 2012).

For this study, spectra of 76 targets in 91 linespec observations were obtained, covering the [O I] 63 μ m and DCO⁺ 190 μ m lines (Table 4). The integration times for the majority of

Table 4
GASPS Taurus Observations: PACS Spectroscopy

Target	R.A. (J2000) (h m s)	Decl. (J2000) (deg m s)	Obs. Mode	Exposure (s)	ObsID
AA Tau	4 34 55.420	+24 28 53.16	LineSpec	1252	1342190357
			LineSpec	6628	1342225758
			RangeSpec	5141	1342190356
			RangeSpec	20555	1342225759
BP Tau	4 19 15.830	+29 06 26.90	LineSpec	1252	1342192796
			LineSpec	3316	1342225728
CIDA 2	4 15 05.157	+28 08 46.21	LineSpec	1252	1342216643
CI Tau	4 33 52.000	+22 50 30.20	LineSpec	1252	1342192125
			RangeSpec	5141	1342192124
CoKu Tau/4	4 41 16.800	+28 40 00.60	LineSpec	1252	1342191360
			LineSpec	6628	1342225837
CW Tau	4 14 17.000	+28 10 57.80	LineSpec	1252	1342216221
			RangeSpec	10279	1342216222
			LineSpec	3316	1342225729
CX Tau	4 14 47.860	+26 48 11.01	LineSpec	1252	1342192794
CY Tau	4 17 33.730	+28 20 46.90	LineSpec	1252	1342192797
DE Tau	4 21 55.640	+27 55 06.10	LineSpec	1252	1342192797
			RangeSpec	8316	1342216648
DF Tau	4 27 03.080	+25 42 23.30	LineSpec	1252	1342190359
			RangeSpec	5141	1342190358
DG Tau	4 27 04.700	+26 06 16.30	LineSpec	1252	1342190382
			RangeSpec	5141	1342190383
			LineSpec	1252	1342192798
DG Tau B	4 27 02.560	+26 05 30.70	RangeSpec	10279	1342196652
			LineSpec	1252	1342225734
DH Tau	4 29 42.020	+26 32 53.20	LineSpec	1252	1342225734
DI Tau ^a	4 29 42.475	+26 32 49.31	LineSpec	1252	1342225734
DK Tau	4 30 44.240	+26 01 24.80	LineSpec	1252	1342192132
			LineSpec	3316	1342225732
			RangeSpec	5141	1342192133
			LineSpec	1252	1342190355
DL Tau	4 33 39.060	+25 20 38.23	LineSpec	6628	1342225800
			RangeSpec	5141	1342190354
			LineSpec	1252	1342192123
			LineSpec	6628	1342225825
DM Tau	4 33 48.720	+18 10 10.00	RangeSpec	5141	1342192122
			LineSpec	1252	1342192127
			LineSpec	3316	1342225757
DN Tau	4 35 27.370	+24 14 58.90	RangeSpec	5141	1342192126
			LineSpec	1252	1342192127
			LineSpec	3316	1342225757
			RangeSpec	5141	1342192126
DO Tau	4 38 28.580	+26 10 49.44	LineSpec	1252	1342190385
			RangeSpec	5141	1342190384
			RangeSpec	12516	1342225802
			LineSpec	1252	1342191362
DP Tau	4 42 37.700	+25 15 37.50	RangeSpec	10279	1342225827
			LineSpec	1252	1342225806
DQ Tau	4 46 53.050	+17 00 00.20	LineSpec	8316	1342225807
			RangeSpec	8316	1342225807
DS Tau	4 47 48.110	+29 25 14.45	LineSpec	3316	1342225851
FF Tau	4 35 20.900	+22 54 24.20	LineSpec	1252	1342192802
FM Tau	4 14 13.580	+28 12 49.20	LineSpec	1252	1342216218
			RangeSpec	10279	1342216219
			LineSpec	1252	1342216645
FO Tau	4 14 49.290	+28 12 30.60	RangeSpec	8316	1342216644
			LineSpec	1252	1342192795
FQ Tau	4 19 12.810	+28 29 33.10	RangeSpec	8316	1342216650
			LineSpec	1252	1342192791
FS Tau	4 22 02.180	+26 57 30.50	LineSpec	1252	1342192791
			RangeSpec	10279	1342194358
FT Tau	4 23 39.190	+24 56 14.10	LineSpec	1252	1342192790
FW Tau	4 29 29.710	+26 16 53.20	LineSpec	1252	1342225735
FX Tau	4 30 29.610	+24 26 45.00	LineSpec	1252	1342192800
GG Tau	4 32 30.350	+17 31 40.60	LineSpec	1252	1342192121
			RangeSpec	5141	1342192120
			RangeSpec	12516	1342225738
GH Tau	4 33 06.430	+24 09 44.50	LineSpec	1252	1342192801
			RangeSpec	8316	1342225762

Table 4
(Continued)

Target	R.A. (J2000) (h m s)	Decl. (J2000) (deg m s)	Obs. Mode	Exposure (s)	ObsID
GI Tau/GK Tau	4 33 34.310	+24 21 11.50	LineSpec	3316	1342225760
GM Aur	4 55 10.990	+30 21 59.25	LineSpec	1252	1342191357
			RangeSpec	5141	1342191356
GO Tau	4 43 03.090	+25 20 18.80	LineSpec	1252	1342191361
			LineSpec	3316	1342225826
Haro 6-5B ^b	4 22 02.18	+26 57 30.5	LineSpec	1252	1342192791
Haro 6-13	4 32 15.410	+24 28 59.70	LineSpec	1252	1342192128
			RangeSpec	5141	1342192129
			RangeSpec	12516	1342225761
Haro 6-37	4 46 58.980	+17 02 38.20	LineSpec	1252	1342225805
HBC 347	3 29 38.370	+24 30 38.00	LineSpec	1252	1342192136
HBC 356	4 03 13.990	+25 52 59.90	LineSpec	1252	1342204134
			LineSpec	1252	1342214359
HBC 358	4 03 50.840	+26 10 53.20	LineSpec	1252	1342204347
			LineSpec	1252	1342214680
HD 283572	4 21 58.847	+28 18 06.51	LineSpec	1660	1342216646
HK Tau	4 31 50.570	+24 24 18.07	LineSpec	3316	1342225736
			RangeSpec	8316	1342225737
HL Tau ^c	4 31 38.437	18 13 57.65	LineSpec	1252	1342190351
HN Tau	4 33 39.350	+17 51 52.37	LineSpec	3316	1342225796
			RangeSpec	10279	1342225797
HO Tau	4 35 20.200	+22 32 14.60	LineSpec	1252	1342192803
HV Tau	4 38 35.280	+26 10 38.63	LineSpec	3316	1342225801
IP Tau	4 24 57.080	+27 11 56.50	LineSpec	3316	1342225756
IQ Tau	4 29 51.560	+26 06 44.90	LineSpec	1252	1342192135
			LineSpec	3316	1342225733
			RangeSpec	5141	1342192134
IRAS 04158+2805	4 18 58.140	+28 12 23.50	LineSpec	1252	1342192793
			RangeSpec	5141	1342192792
IRAS 04385+2550	4 41 38.820	+25 56 26.75	LineSpec	3316	1342225828
			RangeSpec	8316	1342225829
J1- 4872	4 25 17.678	+26 17 50.41	LineSpec	1660	1342216653
LkCa 1	4 13 14.142	+28 19 10.84	LineSpec	1660	1342214679
LkCa 3	4 14 47.973	+27 52 34.65	LineSpec	1660	1342216220
LkCa 4	4 16 28.109	+28 07 35.81	LineSpec	1660	1342216642
LkCa 5	4 17 38.940	+28 33 00.51	LineSpec	1660	1342216641
LkCa 7	4 19 41.272	+27 49 48.49	LineSpec	1660	1342216649
LkCa 15	4 39 17.800	+22 21 03.48	LineSpec	1252	1342190387
			LineSpec	6628	1342225798
			RangeSpec	5141	1342190386
RW Aur	5 07 49.540	+30 24 05.07	LineSpec	1252	1342191359
			RangeSpec	5141	1342191358
RY Tau	4 21 57.400	+28 26 35.54	LineSpec	1252	1342190361
			RangeSpec	5141	1342190360
SU Aur	4 55 59.380	+30 34 01.56	LineSpec	3316	1342217844
			RangeSpec	10279	1342197845
T Tau	4 21 59.430	+19 32 06.37	LineSpec	1252	1342190353
			RangeSpec	5141	1342190352
			LineSpec	1252	1342215699
UX Tau	4 30 03.990	+18 13 49.40	LineSpec	1252	1342204350
			LineSpec	1252	1342214357
UY Aur	4 51 47.380	+30 47 13.50	LineSpec	1252	1342193206
			LineSpec	1252	1342215699
			RangeSpec	10279	1342226001
UZ Tau	4 32 42.890	+25 52 32.60	LineSpec	1252	1342192131
			RangeSpec	5141	1342192130
V710 Tau	4 31 57.800	+18 21 35.10	LineSpec	1252	1342192804
V773 Tau	4 14 12.920	+28 12 12.45	LineSpec	3316	1342216217
V807 Tau ^d	4 33 06.641	+24 09 54.99	LineSpec	1252	1342192801
			RangeSpec	8316	1342225762
V819 Tau	4 19 26.260	+28 26 14.30	LineSpec	1660	1342216651
V836 Tau	5 03 06.600	+25 23 19.70	LineSpec	3316	1342227634

Table 4
(Continued)

Target	R.A. (J2000) (h m s)	Decl. (J2000) (deg m s)	Obs. Mode	Exposure (s)	ObsID
V927 Tau	4 31 23.820	+24 10 52.93	LineSpec	3316	1342225763
V1096 Tau	4 13 27.230	+28 16 24.80	LineSpec	1252	1342214678
VY Tau	4 39 17.410	+22 47 53.40	LineSpec	1252	1342192989
XZ Tau	4 31 39.480	+18 13 55.70	LineSpec	1252	1342190351
			RangeSpec	5141	1342190350
ZZ Tau	4 30 51.380	+24 42 22.30	LineSpec	1252	1342192799

Notes.

- ^a DI Tau observed in the same field of view as DH Tau.
^b Haro 6-5B observed in the same field of view as FS Tau.
^c HL Tau observed in the same field of view as XZ Tau.
^d V807 Tau observed in the same field of view as GH Tau.

observations was 1252 s; a few targets were re-observed with longer integrations ranging from 3316 s to 6628 s. Of the 76 targets observed in linespec mode, 38 were also observed in rangespec mode (42 observations), with integrations of 5141–10279 s, covering 70–200 μm , including the [O I] 145 μm and [C II] 158 μm lines. The spectroscopic data were reduced with HIPE (Ott 2010) v4.2.0, utilizing the pipeline scripts provided at the *Herschel* data reduction workshop in 2010 January.¹⁸

For each observation, we extracted the mean of the two nod positions to obtain flux values for each of the 25 spaxels per observation. We binned the spectra at half the instrumental spectral resolution (Nyquist sampling) for a given wavelength within HIPE, and output standard ASCII text files in order to extract continuum and line flux measurements. We utilized the standard IDL line fitting routine MPFITPEAK (Markwardt 2009) to derive the total line flux and the continuum flux at the observed wavelength of each line. We fit a line to the observed continuum, defined nominally as the region of ~ 2 –10 times the instrumental FWHM from the rest wavelength for each line. The error on the continuum is defined as the standard deviation of the residual about the mean. The reported line fluxes are the integrated flux of a Gaussian line fit, with errors calculated from the errors on the values of line amplitude and width, as reported by MPFITPEAK. For spectra with no line detection we report 3σ upper detection limits, where the 1σ flux is calculated by integrating a Gaussian with height equal to the rms of the continuum and width equal to the instrumental FWHM. Typical rms error values for continuum levels in individual spaxel spectra are ~ 0.05 Jy. Typical line flux errors (rms) are ~ 0.5 – 1×10^{-17} W m⁻².

3.2.2. Correcting PACS Spectroscopy Observations for Pointing Errors

The PACS instrument consists of an array of 25 “spaxels,” arranged 5×5 in a roughly square formation; see Poglitsch et al. Each spaxel subtends $9''.4 \times 9''.4$ on the sky. Ideally, observations are carried out with the celestial source being centered on the central spaxel. For a “well-pointed” observation, the largest flux measured in the spaxel array will, by construction, be located in the central spaxel. In such a case, the total flux of a point source can be estimated from the observed flux in the central spaxel by applying an aperture correction (which is the ratio of the observed flux in the spaxel to the total source flux, as estimated

from the instrument PSF), as provided by the HIPE reduction software.

However, some of the observations for our GASPS OT key program, especially for sources in Taurus, were affected by large errors in the pointing. In some observations the sources were found to be located up to $8''$ from the central spaxel, far greater than reported pointing accuracy¹⁹ of $\sim 2''$. As none of our Taurus sources are extended in continuum emission (cf. Section 3.1), it is clear upon inspection of the relative continuum fluxes in the spaxels of each observation if a source is not well centered (Figure 1). In the case of the GASPS’ Taurus targets, the pointing solution shows the targets systematically to the east of the central spaxel. For these observations, the simple aperture correction method will not yield accurate results, especially since the reduction software provides no way of determining precisely where the source is located relative to the center of the spaxel array. Furthermore, the aperture correction formula makes use of the signal (information) in a single spaxel and ignores any observed flux in any additional spaxels. In order to determine accurately the flux of our targets from these mispointed observations and overcome the shortcomings of the aperture correction formula, we developed a method of estimating the offset of the source from the center of the spaxel array, and using that information to calculate an “optimum” value of the source flux.

To do this, we simulated the observation of a source using wavelength-appropriate theoretical PACS PSFs²⁰ and the known spaxel sizes and locations relative to the central spaxel. The theoretical PSFs are very close to the observed PSFs (see Poglitsch et al. 2010), deviating from the observed PSFs on the order of only a few percent. Relative spaxel positions on the sky are obtained from the R.A. and decl. coordinates provided for each spaxel in HIPE. We take into account the position angle (P.A.) of the telescope to transform the spaxel offsets from R.A. and decl. to arcseconds in (y , z) spacecraft coordinates.

The simulations consisted of computing, for each spaxel, the fractional flux as well as the flux relative to the “observed” peak flux as a function of offset in spacecraft coordinates (y and z) between the peak of the PSF and the center of the spaxel array. We stepped the spaxel array across the wavelength appropriate theoretical PSFs, generating a library of spaxel fractional fluxes and relative fluxes for offsets of $\pm 20''$, in increments of $0''.5$, in both directions. For any given observation, the continuum fluxes in each spaxel were divided by the peak continuum value

¹⁸ <https://nhscsci.ipac.caltech.edu/sc/index.php/~Workshops/>

¹⁹ <http://herschel.esac.esa.int/twiki/bin/view/Public/SummaryPointing>

²⁰ <http://pacs.ster.kuleuven.ac.be/pubtool.psf>

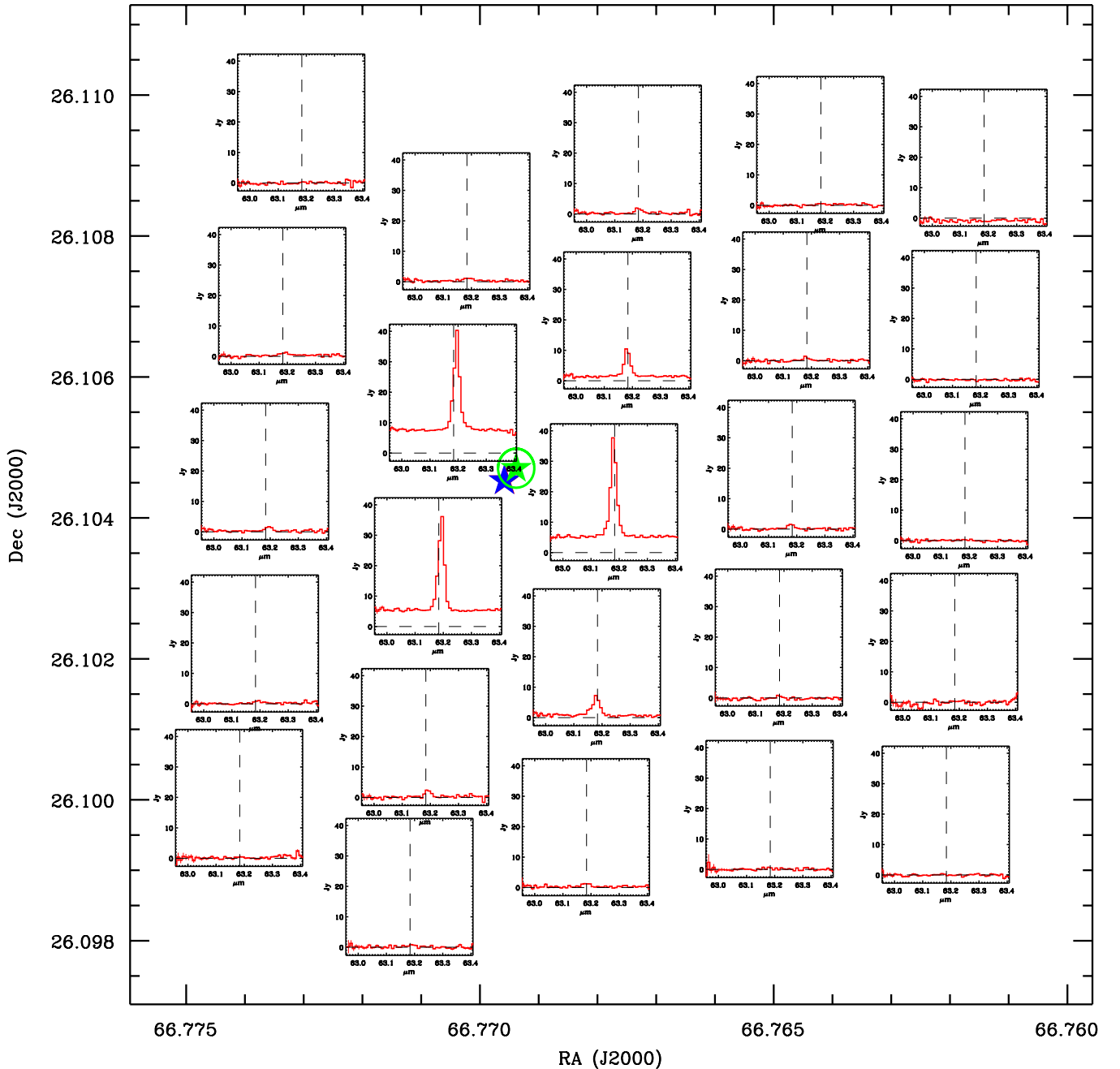


Figure 1. “Footprint” for DG Tau. Spaxels are plotted as $7''$ on a side for clarity. Because DG Tau is not extended in continuum at $63\ \mu\text{m}$, it is easily identified as falling off the central spaxel by examining the relative continuum values in each spaxel. Plotted as the green star is the best fit position of the target via χ^2 minimization of spaxel continuum values and the theoretical PSF at $63\ \mu\text{m}$. A $1''$ error circle representing the error in the positional fit is plotted. The blue star is the SIMBAD position for DG Tau.

(A color version of this figure is available in the online journal.)

and then compared to the simulated relative fluxes at each offset position in the library using a χ^2 statistic. The positional offset (relative to the central spaxel) of the source is given by the offset location that yielded the minimum χ^2 . As in the line fits, the region used to define the continuum in each spaxel was a range ~ 2 – 10 times the instrumental FWHM from the rest wavelength for each line.

Once the offset position was known, the fractional fluxes corresponding to that offset were used to estimate the optimal value of the total source flux (see, e.g., Horne 1986). For the best fit offset position, we calculated an optimal flux value via

an error weighted average using only spaxels with a detected flux level above a signal-to-noise ratio (S/N) greater than 5. The optimal estimate is given by

$$F_{\text{opt.}} = \frac{\sum_{i=0}^n w_i \cdot f_i}{\sum_{i=0}^n w_i} \quad (1)$$

with an error of

$$\sigma_{\text{opt.}} = \left(\sum_{i=0}^n w_i \right)^{-1/2}. \quad (2)$$

The w_i are weights given by

$$w_i = \frac{1}{(\sigma_i/p_i)^2}, \quad (3)$$

where p_i is the fractional flux in spaxel i as given by the previous determination of the offset, and σ_i is the measured statistical error (the standard deviation on the mean continuum, as described above) on the continuum flux. For bright sources, several spaxels contribute to the final flux estimate, with each contribution weighted by the fractional flux in that spaxel for the estimated offset position. For weak sources, or those that are well centered in a single spaxel (and therefore, for which flux is detected in only a single spaxel), the method should give the same result as the simple aperture correction formula. A comparison of our “optimum” flux estimates and fluxes using the single spaxel and the aperture correction value provided by HIPE, for well-centered sources shows the values to be equivalent (i.e., for well-centered sources, or faint sources where flux is seen in only a single spaxel, the method of “optimal” flux estimates described herein is consistent with standard flux estimates utilizing only the HIPE reduction method).

For targets in which two sources were present in the PACS field of view (ObsID 1342192193 containing FS Tau A/B, ObsID 1342190351 containing XZ and HL Tau, ObsID 1342192801 containing V807 Tau and GH Tau), the method described above was modified somewhat to account for additional flux from each source in each spaxel. The spaxels with the peak fluxes, corresponding to the approximate locations of the sources, were identified. For each individual source in the field of view, the method described above was carried out after setting the weights for all spaxels between the two peaks and those associated with the other source to zero. As above, the total flux of the sources was then determined from a least-squares fit of the predicted fluxes in the remaining spaxels to the observed fluxes. This yielded accurate relative locations, and thus accurate continuum flux values, of the two sources in each field of view.

Testing of the code was performed on sources falling off the central spaxel (as determined from “by-eye” inspection of relative continuum values) as well as on well-centered sources. The positional uncertainties in the y, z offsets, as defined by a 1σ confidence contour based on the χ^2 minimization, are less than $0.5''$ in radial offset, which is less than our step increments used in generating the fractional fluxes falling in each spaxel. As an additional check of the offset code, we find very good agreement in derived offset positions between different wavelengths (linespec and rangespec observations), which are separate observations, but usually done back to back and which show the same pointing anomalies. From a sample of 19 targets obtained in both spectroscopy modes (line scan and range scan), we find agreement in derived radial offset positions computed using the 7 different wavelength ranges, to be better than $1''$ in radial offset.

As described above, all spectroscopy continuum values reported herein are the result of the error weighted average of the aperture corrected flux in spaxels which have a S/N of 5 or greater. Only one T Tauri star, T Tau itself, is extended at PACS wavelengths; millimeter interferometry of many of the Taurus sources (Andrews & Williams 2007; Isella et al. 2009; Guilloteau et al. 2011; Harris et al. 2012) show the disk diameters to be $<2''$ on the sky. Since the observed sizes of the objects in our sample will be smaller at the PACS wavelengths of 60–200 μm than at millimeter wavelengths, any “extended”

continuum emission in multiple spaxels above and beyond what would be expected from the PSF (i.e., adjacent spaxels with equal continuum measurements) is a result of mis-pointing of the telescope.

However, the line emission can often be somewhat extended, especially for young T Tauri stars, as many of the sources in our sample are well-studied outflow sources. In disks surrounding stars with known outflows, summing the line flux contribution from all spaxels will overestimate the line emission arising from the disk, since the spectral and spatial resolution of PACS at these wavelengths is insufficient to resolve the outflow component of the line emission from that of the disk. Therefore, the observed [O I] 63 μm emission in outflow sources only provides an upper limit to the emission from the disk. To minimize the contribution from the outflow, we only quote the line intensity from the central spaxel (well-centered observations) or the expected line intensity at the continuum peak interpolated from the line intensities in nearby spaxels. This is only significant for spatially extended sources like T Tau and DG Tau B, where our line intensities are about a factor of two smaller than the total (i.e., spatially integrated) line intensities reported by Podio et al. (2012).

3.2.3. Comparison of Spectroscopy and Photometry

We compare the continuum flux values obtained from photometry (Table 1) with those from spectroscopy (Table 5) in Figure 2. The photometric calibration for PACS has been shown to have much higher absolute accuracy than the spectroscopic calibration (Vandenbussche et al. 2011; Müller et al. 2011). We find that the photometry continuum values are consistently higher by $\sim 30\text{--}40\%$ (rms $\sim 20\%$) than the spectroscopic values at both 70 and 100 μm . This calibration discrepancy appears to be wavelength dependent; comparison of the 160 μm photometric continuum and the 158 μm spectroscopic continuum values show agreement to within 2% (rms $\sim 20\%$), on average. We consider the absolute calibration of the spectroscopic data reduced with HIPE v4.2.0 to be accurate to within $\sim 40\%$.

In order to check how much the calibration has improved in the most recent HIPE release, v10.0, we re-reduced the spectra at 63 μm for a randomly selected sample of 15 stars ranging from very faint, i.e., continuum emission ≤ 0.5 Jy at 63 μm , intermediate (a few Jy), to bright (10 Jy) with about five stars in each category. The HIPE v10.0 calibration has certainly improved and is much closer to the results obtained from continuum photometry. From the comparison sample we find that the continuum flux densities are 18% brighter in HIPE v10.0 than compared to HIPE v4.2, while the line intensities are only 11% brighter than in HIPE v4.2. Within errors, however, there is no clear difference between continuum and line calibration. For very faint sources HIPE v10.0 is no better than HIPE v4.2, for both releases the spectroscopy calibration can be off by more than 50% compared to each other and to very accurate photometry.²¹ Since we have overlapping targets with the DIGIT project (Sturm et al. 2010), we also compared the targets in common; the well-pointed DIGIT observations agree extremely well with our photometry. In general we find agreement to better than 15% when comparing spectra reduced in HIPE v4.2 to that

²¹ All spectroscopy and photometry will be re-reduced by the GASPS team as part of our data delivery once HIPE is stable. This is expected to change the overall calibration for the spectroscopy bands B2A and B2B (50–70 μm) by $\sim 20\%$; for all other spectroscopy bands and for photometry the changes are expected to be small.

Table 5
Continuum Flux in Spectroscopic Observations

Name	63.18 μm (Jy)	72.84 μm (Jy)	78.74 μm (Jy)	90.16 μm (Jy)	145.53 μm (Jy)	157.74 μm (Jy)	179.53 μm (Jy)	189.57 μm (Jy)
AA Tau	0.85 ± 0.02	0.85 ± 0.02	0.82 ± 0.02	0.89 ± 0.01	0.99 ± 0.01	1.18 ± 0.01	1.12 ± 0.02	0.92 ± 0.05
BP Tau	0.45 ± 0.04	<0.17
CI Tau	1.38 ± 0.05	1.62 ± 0.03	1.57 ± 0.05	1.90 ± 0.04	2.04 ± 0.03	2.37 ± 0.03	2.52 ± 0.04	2.06 ± 0.07
CIDA 2	<0.09	<0.24
CoKu Tau-4	0.90 ± 0.02	0.61 ± 0.04
CW Tau	1.31 ± 0.04	1.48 ± 0.03	1.58 ± 0.02	1.59 ± 0.03	1.67 ± 0.02	1.93 ± 0.02	1.83 ± 0.02	1.81 ± 0.10
CX Tau	0.30 ± 0.03	<0.22
CY Tau	<0.15	<0.29
DE Tau	1.35 ± 0.05	0.70 ± 0.03	0.67 ± 0.02	...	0.65 ± 0.01	0.62 ± 0.01	...	<0.27
DF Tau	0.43 ± 0.05	0.32 ± 0.03	0.35 ± 0.04	0.59 ± 0.04	0.20 ± 0.02	0.12 ± 0.03	0.20 ± 0.04	<0.29
DG Tau	13.94 ± 0.09	11.94 ± 0.04	13.72 ± 0.07	14.87 ± 0.04	14.09 ± 0.03	15.27 ± 0.03	14.26 ± 0.05	11.54 ± 0.06
DG Tau B	9.85 ± 0.05	10.37 ± 0.03	10.96 ± 0.04	11.79 ± 0.03	14.63 ± 0.02	15.34 ± 0.02	14.46 ± 0.03	13.88 ± 0.09
DH Tau	0.25 ± 0.05	0.39 ± 0.07
DI Tau	<0.15	<0.22
DK Tau	0.86 ± 0.03	0.73 ± 0.04	0.73 ± 0.04	0.90 ± 0.05	0.76 ± 0.03	0.85 ± 0.03	1.04 ± 0.04	<0.31
DL Tau	0.96 ± 0.02	0.71 ± 0.03	1.07 ± 0.05	1.08 ± 0.05	1.49 ± 0.02	1.77 ± 0.03	2.15 ± 0.04	1.58 ± 0.03
DM Tau	0.58 ± 0.02	0.68 ± 0.03	0.86 ± 0.04	0.81 ± 0.03	0.81 ± 0.03	0.93 ± 0.02	1.04 ± 0.04	0.65 ± 0.03
DN Tau	0.69 ± 0.02	0.55 ± 0.05	0.70 ± 0.05	0.58 ± 0.04	0.63 ± 0.02	0.77 ± 0.03	0.78 ± 0.04	0.70 ± 0.06
DO Tau	2.82 ± 0.05	4.01 ± 0.02	4.16 ± 0.02	3.15 ± 0.04	3.94 ± 0.01	4.27 ± 0.01	3.45 ± 0.04	2.87 ± 0.07
DP Tau	0.79 ± 0.06	0.36 ± 0.02	0.32 ± 0.03	0.37 ± 0.02	0.18 ± 0.02	0.25 ± 0.02	0.32 ± 0.03	<0.31
DQ Tau	1.14 ± 0.04	1.13 ± 0.02	1.18 ± 0.02	...	0.98 ± 0.01	1.09 ± 0.02	...	0.64 ± 0.09
DS Tau	0.17 ± 0.03	<0.17
FF Tau	<0.12	<0.29
FM Tau	0.56 ± 0.06	0.39 ± 0.02	0.39 ± 0.02	0.59 ± 0.03	0.23 ± 0.02	0.30 ± 0.02	0.26 ± 0.02	<0.29
FO Tau	0.42 ± 0.05	0.35 ± 0.02	0.39 ± 0.02	...	0.23 ± 0.01	0.26 ± 0.01	...	<0.23
FQ Tau	<0.12	0.11 ± 0.02	0.15 ± 0.02	...	0.06 ± 0.01	0.09 ± 0.01	...	<0.32
FS Tau A	2.34 ± 0.05	1.73 ± 0.03	1.61 ± 0.07	1.88 ± 0.03	1.63 ± 0.02	1.78 ± 0.02	1.55 ± 0.03	1.47 ± 0.09
FT Tau	0.52 ± 0.04	1.06 ± 0.11
FW Tau	<0.12	<0.29
FX Tau	0.17 ± 0.05	<0.29
GG Tau Aab	2.93 ± 0.04	3.97 ± 0.01	4.51 ± 0.03	4.52 ± 0.04	7.62 ± 0.01	8.60 ± 0.01	8.22 ± 0.03	7.13 ± 0.08
GH Tau	0.87 ± 0.05	0.34 ± 0.02	0.30 ± 0.02	...	0.18 ± 0.02	0.20 ± 0.01	...	0.31 ± 0.07
GI/GK Tau ^a	0.91 ± 0.07	0.82 ± 0.12
GM Aur	1.99 ± 0.05	2.46 ± 0.05	2.46 ± 0.04	3.00 ± 0.04	3.64 ± 0.02	4.25 ± 0.03	5.00 ± 0.04	2.78 ± 0.07
GO Tau	0.24 ± 0.02	0.50 ± 0.04
Haro6-5B	2.11 ± 0.05	1.87 ± 0.02	1.68 ± 0.03	1.79 ± 0.03	2.26 ± 0.02	2.61 ± 0.02	2.66 ± 0.03	3.73 ± 0.10
Haro 6-13	5.04 ± 0.05	5.53 ± 0.05	6.59 ± 0.02	5.84 ± 0.04	6.37 ± 0.01	6.86 ± 0.02	6.55 ± 0.05	5.41 ± 0.08
Haro 6-37	0.85 ± 0.04	1.42 ± 0.07
HBC 347	<0.15	<0.32
HBC 356	<0.09	<0.24
HBC 358	<0.18	<0.29
HD 283572	<0.09	<0.22
HK Tau	2.03 ± 0.03	2.13 ± 0.02	2.29 ± 0.02	...	2.13 ± 0.01	2.43 ± 0.01	...	1.73 ± 0.07
HL Tau	66.19 ± 0.14	65.15 ± 0.07	65.98 ± 0.08	67.79 ± 0.08	65.91 ± 0.06	69.37 ± 0.08	53.90 ± 0.09	45.45 ± 0.11
HN Tau	0.77 ± 0.02	0.71 ± 0.02	0.79 ± 0.03	0.74 ± 0.03	0.60 ± 0.01	0.64 ± 0.02	0.60 ± 0.03	0.55 ± 0.07
HO Tau	<0.12	<0.34
HV Tau C	0.80 ± 0.04	1.09 ± 0.05
IP Tau	0.44 ± 0.03	<0.16
IQ Tau	0.61 ± 0.03	0.48 ± 0.06	0.43 ± 0.03	0.59 ± 0.04	0.59 ± 0.02	0.70 ± 0.03	0.76 ± 0.04	0.71 ± 0.06
IRAS 04158+2805	0.76 ± 0.05	0.92 ± 0.03	0.93 ± 0.04	1.25 ± 0.05	2.45 ± 0.02	3.18 ± 0.03	3.87 ± 0.03	2.94 ± 0.08
IRAS 04358+2550	1.87 ± 0.02	1.44 ± 0.04
J1-4827	<0.09	<0.27
LkCa 1	<0.09	<0.26
LkCa 3	<0.12	<0.27
LkCa 4	0.12 ± 0.04	<0.22
LkCa 5	<0.12	<0.24
LkCa 7	<0.12	<0.20
LkCa 15	0.99 ± 0.02	0.98 ± 0.04	1.08 ± 0.04	1.13 ± 0.04	1.55 ± 0.03	1.82 ± 0.03	2.18 ± 0.06	1.28 ± 0.04
RW Aur	1.79 ± 0.05	1.85 ± 0.04	2.09 ± 0.04	2.04 ± 0.04	1.30 ± 0.02	1.54 ± 0.03	1.41 ± 0.04	1.12 ± 0.13
RY Tau	10.86 ± 0.07	9.82 ± 0.03	10.10 ± 0.04	10.00 ± 0.04	7.98 ± 0.02	8.64 ± 0.03	8.50 ± 0.04	5.73 ± 0.11
SU Aur	5.95 ± 0.02	5.44 ± 0.02	4.72 ± 0.03	4.11 ± 0.03	3.24 ± 0.02	3.33 ± 0.02	2.10 ± 0.02	1.49 ± 0.05
T Tau	86.12 ± 0.21	77.48 ± 0.07	75.93 ± 0.10	67.18 ± 0.15	39.53 ± 0.26	39.64 ± 0.06	35.77 ± 0.23	25.28 ± 0.13
UX Tau	3.28 ± 0.03	2.31 ± 0.07
UY Aur	4.85 ± 0.06	4.87 ± 0.02	4.89 ± 0.04	4.52 ± 0.04	3.11 ± 0.01	3.30 ± 0.02	2.39 ± 0.02	2.11 ± 0.07
UZ Tau	1.23 ± 0.06	1.29 ± 0.04	1.47 ± 0.05	1.38 ± 0.04	1.78 ± 0.03	1.94 ± 0.02	1.69 ± 0.04	1.54 ± 0.09

Table 5
(Continued)

Name	63.18 μm (Jy)	72.84 μm (Jy)	78.74 μm (Jy)	90.16 μm (Jy)	145.53 μm (Jy)	157.74 μm (Jy)	179.53 μm (Jy)	189.57 μm (Jy)
V710 Tau	0.47 \pm 0.05	1.10 \pm 0.18
V773 Tau	0.66 \pm 0.03	<0.17
V807 Tau	0.58 \pm 0.05	0.13 \pm 0.02	0.12 \pm 0.02	...	0.17 \pm 0.02	0.18 \pm 0.02	...	<0.29
V819 Tau	<0.12	<0.22
V836 Tau	0.33 \pm 0.02	0.27 \pm 0.04
V927 Tau	<0.09	<0.17
V1096 Tau	<0.15	<0.27
VY Tau	<0.12	<0.29
XZ Tau	4.20 \pm 0.05	3.98 \pm 0.04	4.04 \pm 0.06	3.89 \pm 0.04	2.90 \pm 0.02	2.78 \pm 0.03	2.87 \pm 0.06	3.71 \pm 0.08
ZZ Tau	<0.12	<0.29

Note. ^a Gi Tau and GK Tau are unresolved in spectroscopy.

of the DIGIT project, except for DG Tau, where the discrepancy is 50% (G. Herczeg 2011, private communication).

The spectroscopic data in this paper are presented as a self-consistent dataset, completely reduced with HIPE v4.2 in order to avoid confusion regarding scaling values for targets reduced with different versions of HIPE. As the main results of this paper focus on comparison of continuum and line flux values at a given wavelength, the results should be unaffected by an overall scaling of line and continuum flux values, except possibly for line ratio values (discussed in Section 4.4). We note that in principle both the continuum and line intensities should be scaled by the appropriate value as determined by comparison to photometry for those wishing to use the continuum or line flux values contained herein. However, as there is not a 100% overlap between sources observed in photometry and spectroscopy modes, and because of the wavelength dependence of the calibration, none of the spectroscopic continuum and line flux values (and corresponding plots) in this paper has been scaled to match those obtained by photometry.

4. RESULTS OF SPECTROSCOPY

Table 2 lists the [O I] 63 μm , [O I] 145 μm , and [C II] 158 μm line flux values for our GASPS Taurus sample. The PACS spectroscopy continuum values are listed in Table 5. In some of our targets, other molecular lines like OH, CH⁺, and CO (for a complete listing, see Table 3) are also seen, primarily in known outflow sources (see, e.g., Podio et al. 2012). The o-H₂O line at 63.323 μm is also detected in eight of the sources in our sample (Riviere-Marichalar et al. 2012). This water line is only seen in outflow sources, although the emission is thought to originate in the disk rather than in the outflow. Although discussion of these molecular lines is outside the scope of this paper, targets which show evidence of these various molecular lines are noted in Table 2. Here we discuss only the strongest lines seen in the GASPS spectroscopic sample, i.e., the two [O I] lines and the [C II] line, which dominate the gas cooling (Tielens & Hollenbach 1985).

4.1. [O I] 63 μm Emission

The [O I] 63 μm line was observed in 76 fields (Table 4) and detected in 43 stars at 3σ or more. It was seen in all Class I objects, and in most Class II sources and transitional disk systems. We found that we always detected the [O I] 63 μm line at $\geq 3\sigma$ if the 63 μm continuum flux was ≥ 0.5 Jy. The line is seen in known outflow sources as well as in “disk-only” and

transitional disk systems. For outflow sources, the [O I] 63 μm line emission is essentially compact, whereas the jets seen in H α or in forbidden optical lines often trace the outflow over one or several arcminutes from the star. The emission can be slightly extended in strong outflow sources (cf. Podio et al. 2012). Line flux values in our sample range from 10^{-17} W m⁻² (our sensitivity limit) to $\sim 5 \times 10^{-17}$ W m⁻² for sources with no evidence of outflow and up to almost 10^{-14} W m⁻² for known outflow sources.

4.2. [O I] 145 μm Emission

The [O I] 145 μm line, with an energy level of ~ 327 K, is more difficult to detect than the transition at 63 μm . We detect the 145 μm line at $\geq 3\sigma$ in 17 objects, nearly all of them outflow sources (Table 2); only one is a disk object. The non-detections of our disk sources show that the [O I] 145 μm line is more than 10 times fainter than the [O I] 63 μm line in the disk. DE Tau is an exception, here the 145 μm line is about as strong as the 63 μm line, see Section 5.7. This does not mean that the [O I] 145 μm emission is absent in disks, but since our disk sources are relatively faint, the expected line emission is generally below our detection limit, see Section 4.4. Figure 3 shows three examples of the [O I] 145 μm line detections in our sample.

4.3. [C II] 158 μm Emission

For the [C II] 158 μm line the detection rate is even lower than for the [O I] 145 μm line; only 10 targets were detected, all of them outflow sources. Figure 4 shows three examples of [C II] 158 μm spectra. Previous *Infrared Space Observatory (ISO)* observations (Creech-Eakman et al. 2002; Nisini et al. 2002; Liseau et al. 2006) show strong ($\sim 10^{-16}$ to 10^{-15} W m⁻²) [C II] 158 μm emission in young (mostly Class 0 and Class I) stellar objects. The [C II] is likely to originate in the outflow, rather than in the disk. In the sample of strong outflow sources studied by Podio et al. (2012), they found that the [C II] emission was somewhat extended compared to the continuum emission from the disk for all but one source in their sample. In the prototypical outflow source HH 46 observed with PACS, van Kempen et al. (2010) found that the [C II] emission was twice as strong in the blue-shifted outflow compared to the red-shifted outflow lobe or to the spaxel centered on the protostar, demonstrating that most, if not all of the [C II] emission originates in the outflow rather than in the disk.

For the outflow sources in our sample, we see [C II] 158 μm line fluxes of $\sim 10^{-17}$ W m⁻² (DG Tau B and T Tau stand out with [C II] 158 μm line flux values of $\sim 10^{-16}$ W m⁻²),

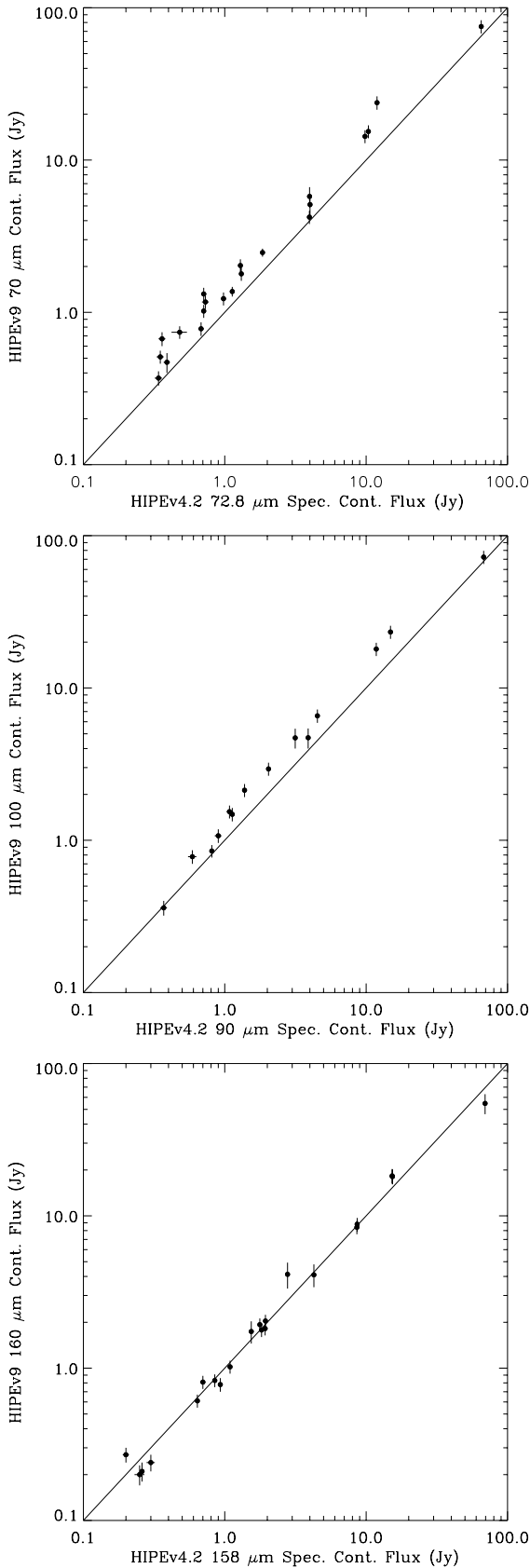


Figure 2. Comparison of PACS photometric values obtained with HIPEv9 and PACS spectroscopic values obtained with HIPEv4.2. Top: 70 μm photometry vs. 72.8 μm spectroscopy. The photometric values at 70 μm are systematically $\sim 42\%$ (rms $\sim 26\%$) higher than spectroscopy. Middle: at 100 μm the photometric values are $\sim 33\%$ (rms $\sim 20\%$) higher than spectroscopy. Bottom: at 160 μm and the photometric and spectroscopy values agree to within $\sim 2\%$ (rms $\sim 20\%$), on average.

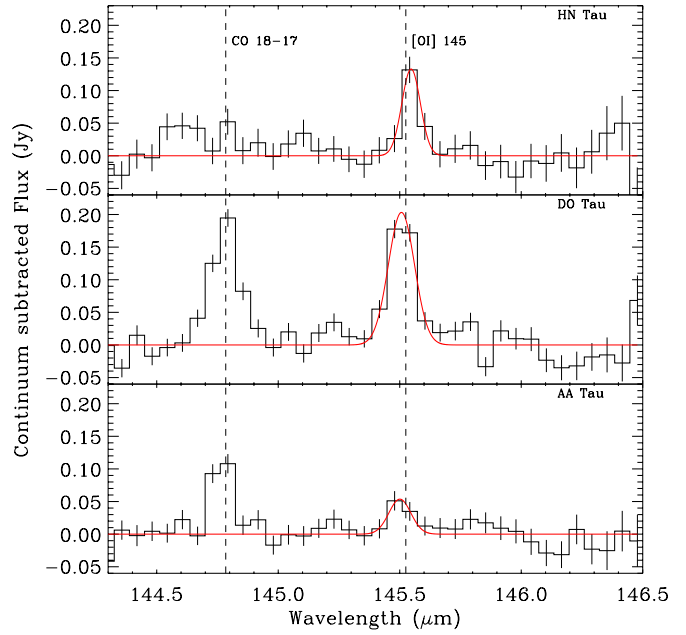


Figure 3. [O I] 145 line detections for three of the targets in the Taurus sample. The line at 144.784 μm is CO $J = 18 \rightarrow 17$. (A color version of this figure is available in the online journal.)

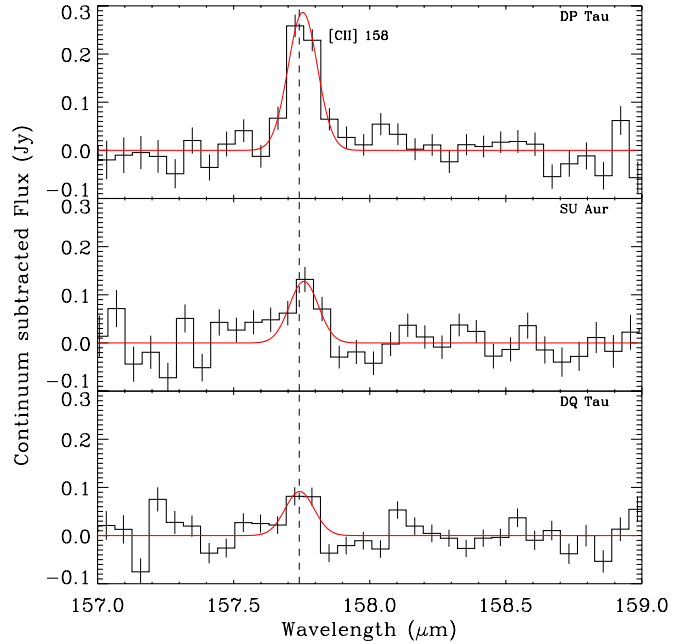


Figure 4. [C II] 158 line detections for three of the targets in the Taurus sample. DQ Tau (bottom panel) is a non-detection. The line seen at $\lesssim 2\sigma$ is almost certainly spurious.

(A color version of this figure is available in the online journal.)

more than an order of magnitude lower than the previous *ISO* observations. Because the *ISO* beam was very large at 158 μm , $\sim 80''$, it is likely that *ISO* picked up extended low surface brightness emission from the surrounding cloud or emission from unrelated sources.

4.4. Line Ratios

Figure 5 shows the line ratios for [O I] 63 μm , [O I] 145 μm , and [C II] 158 μm . In all cases where the lines are detected at 3σ or higher, the line ratios are 10–25 for [O I] 63/[O I] 145. The line ratios for [O I] 63/[C II] 158 are similar. Due to the wavelength

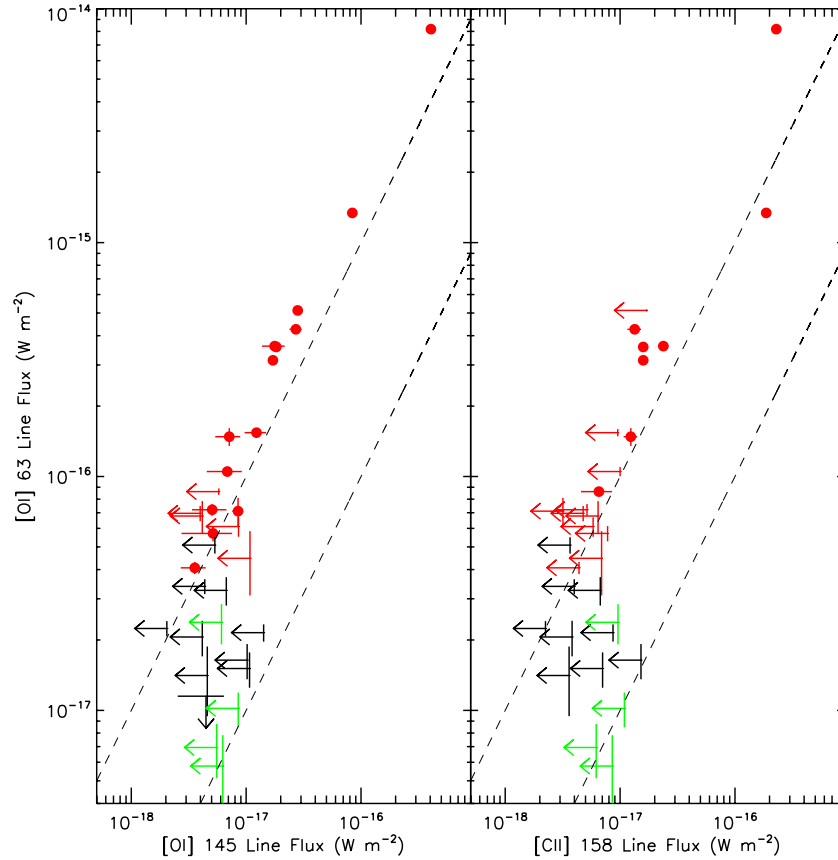


Figure 5. [O I] 63 μm vs. [O I] 145 μm (left) and [C II] 158 μm (right) line flux for the targets in the Taurus sample. Solid circles are sources for which there is a $\geq 3\sigma$ detection for the lines. Sources for which the line detection is $< 3\sigma$ are plotted as 3σ upper limits. Red points are known outflow sources, black non-outflow, and green are transitional disks. The lower dashed line corresponds to a ratio of one, and the upper dashed line to a ratio of 10. Left: all of the outflow sources show ratios of ~ 10 or higher, whereas the non outflow sources are typically undetected in [O I] 145 μm , with the exception of DE Tau.

(A color version of this figure is available in the online journal.)

dependence on calibration with spectroscopy (discussed in Section 3.2.3), these ratios are likely to be even higher, as the [O I] 63 μm line flux is systematically underestimated in comparison to the [O I] 145 μm and [C II] 158 μm line fluxes.

4.5. 63 μm Continuum versus [O I] 63 μm Emission

Since the [O I] 63 μm line can be strong in outflows, we divided our sample into two sets: (1) the “disk-only” stars, where the star has no or only weak outflow activity and (2) jet/outflow sources, where there is clear evidence for outflow activity (see Section 2). In Figure 6 we plot the [O I] 63 μm line intensities versus the 63 μm continuum flux density. We find a tight correlation between [O I] line emission and 63 μm continuum flux with a correlation coefficient of 0.90 for the disk sources which have both line and continuum fluxes $> 3\sigma$. A weighted fit gives

$$\log(\text{O I}) = (0.737 \pm 0.06) \times \log(S_{63}) - (0.22 \pm 0.02), \quad (4)$$

where O I is the [O I] 63 μm line flux in $10^{-16} \text{ W m}^{-2}$ and S_{63} is the continuum flux in Jy at 63 μm . This fit is shown as a black line in Figure 6. Our typical 3σ line detection limits, $\sim 10^{-17} \text{ W m}^{-2}$, are not stringent enough to conclusively determine if the trend continues to values below ~ 0.3 Jy. All transitional disks lie below the correlation. In order to verify this correlation is valid beyond the 12 detected disk-only sources, we have used Kendall’s Rank Correlation, a correlation statistic that accounts for non-detections, but does not include uncertainties

on detected sources (Isobe et al. 1986). We use an IDL adaptation of the algorithm presented in Isobe et al. (1986) to carry out the calculation. The population of 12 detected sources have a Z -value of 3.57, indicating there is a 3.6×10^{-4} probability that a correlation is not present. When all 40 disk-only objects are included, the Z -value increases to 5.29, indicating that the probability of no correlation is essentially 0.

Furthermore, we carry out a log–log fit to the fluxes and 3σ upper limits of all disk-only sources. This fit is a modified χ^2 minimization using the Levenburg–Marquardt algorithm as implemented in the IDL code MPFIT (Markwardt 2009). For detections, the contribution to χ^2 is determined as normal (i.e., $((O - M)/\sigma)^2$). For non-detections, the χ^2 value is set such that if the model value is below the 4σ limit, the point contributes a value of 1 to the deviates. For values above 4σ , the χ^2 value is calculated as if the object were detected at the 3σ value with an uncertainty of 1σ . Parameter uncertainties from this procedure are lower-limits, and do not reflect the two-sided nature of the uncertainties.

This log–log fit results in a slightly shallower slope, 0.69 ± 0.04 , but is still well within the 1σ errors. These tests of the correlation and the line-fit to the disk-only locus confirm that the line flux and the 63 μm flux are strongly correlated.

While the outflow sources show a similar trend, i.e., that sources with higher continuum flux tend to have higher line flux, they can exhibit line fluxes that are up to ~ 20 times higher than non-outflow sources for a given continuum value. For these outflow sources, it is clear that the [O I] 63 μm line emission is

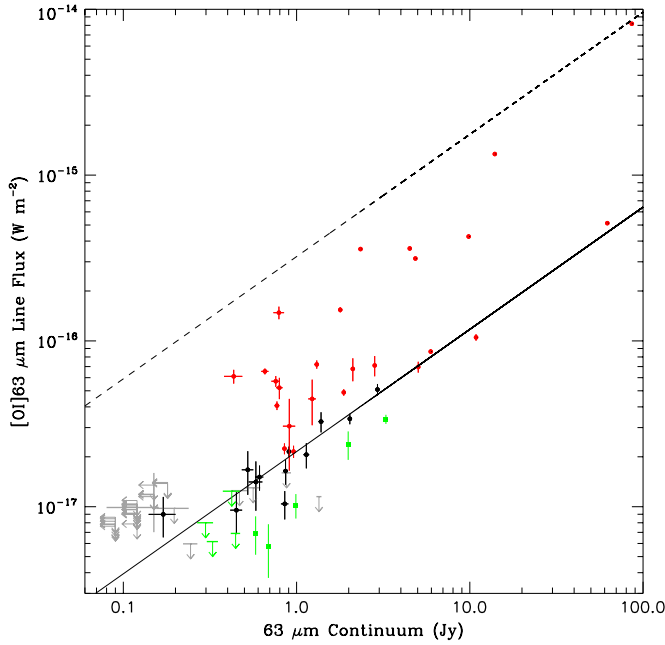


Figure 6. [O I] $63\ \mu\text{m}$ line emission vs. $63\ \mu\text{m}$ continuum emission for the GASPS Taurus sample. Non-outflow sources are plotted in black, outflow sources are plotted in red, and transitional disks are plotted in green. Sources for which there is less than 3σ detection in line flux or continuum are plotted in gray as 3σ upper limits. None of the sources plotted in gray are known to drive outflows. There is a tight correlation (lower black line) between [O I] line emission and $63\ \mu\text{m}$ continuum flux for non-outflow sources (sources with less than 3σ detection in line or continuum flux (the known outflow sources and the transitional disks were omitted from the line fit), suggesting that the emission originates from the same part of the disk. The [O I] $63\ \mu\text{m}$ line emission in outflow sources is dominated by the outflow, and can be up to 20 times stronger (upper dashed line) than the emission from the disk.

(A color version of this figure is available in the online journal.)

completely dominated by the outflow. However, there are some outflow sources, which lie along the best-fit line to the disk-only sources (6 out of 24), suggesting that in some cases the shocks in the jets are not strong enough to excite the [O I] $63\ \mu\text{m}$. Nevertheless, the strong correlation between [O I] emission and $63\ \mu\text{m}$ continuum for disk sources suggests that one may use low spectral resolution [O I] observations to determine whether a PMS star drives an outflow or use the derived correlation to provide a rough estimate of how much of the [O I] $63\ \mu\text{m}$ line emission originates in the disk.

Several sources in our sample were detected in continuum emission at $63\ \mu\text{m}$ but showed little (below 3σ) or no [O I] $63\ \mu\text{m}$ line emission in our first set of observations. Some of the sources for which there was a hint of a line were re-observed with roughly three times the exposure, yielding line detections on the order of $0.5\text{--}1 \times 10^{-17}\ \text{W m}^{-2}$ as shown in Figure 6. All the sources, which were re-observed, were detected. For several re-observed sources, the line flux is lower than what the correlation would predict. Some of these sources, however, are known transitional systems (DM Tau, DN Tau, UX Tau A, GM Aur, and LkCa 15), which we already identified as having weaker [O I] line intensities than CTTs for the same continuum flux. This result suggests that the correlation between line flux and continuum is not only a good indicator of whether a source drives an outflow, but can also serve as a diagnostic for transitional disks. These transitional disks will be discussed in detail in a forthcoming paper (F. Ménard et al. 2013, in preparation).

If we include marginal line detections, i.e., $>2\sigma$ but $<3\sigma$, we find an additional seven sources which lie below the correlation for “disk-only” sources. Four of these marginal detections are transitional disks (FO Tau, CX Tau, IP Tau, and V836 Tau; Najita et al. 2007; Espaillat et al. 2011; Furlan et al. 2011), which confirm the trend we already saw, i.e., transitional disks are intrinsically fainter in [O I] $63\ \mu\text{m}$ than classical disks. The remaining three (Haro 6-37, FM Tau, and V710 Tau; see Table 2) may be entering the transitional phase of their evolution, or alternatively they appear faint due to increased systematic errors for faint sources.

One other source stand out, GH Tau. It has a continuum flux density of 0.8 Jy at $63\ \mu\text{m}$ (Table 5), yet the [O I] $63\ \mu\text{m}$ line emission is less than 3σ . However, at $70\ \mu\text{m}$ the flux density is only 0.37 Jy (Table 1). Therefore the continuum emission at $63\ \mu\text{m}$ is overestimated by more than a factor of two, and the [O I] $63\ \mu\text{m}$ 2σ detection is at the level we would expect.

5. DISCUSSION

5.1. [O I] $63\ \mu\text{m}$ Emission

The [O I] $63\ \mu\text{m}$ line, with an upper energy level of 228 K, is one of the strongest FIR lines observed in the PACS wavelength range and a dominant cooling transition. Emission is thought to arise from the surface region of almost the entire disk (Gorti et al. 2011; Kamp et al. 2011) with 50% of the emission coming from outside of 100 AU (Kamp et al. 2010). Meijerink et al. (2012) find the bulk of the atomic oxygen to be in LTE, and hence the [O I] $63\ \mu\text{m}$ and $145\ \mu\text{m}$ lines should be sensitive to the average temperature of the emission regions they are probing, making them potential probes of the energy of the gas. Several models show that the [O I] $63\ \mu\text{m}$ line is optically thick everywhere in the disk (Gorti & Hollenbach 2008; Kamp et al. 2011).

Thermo-chemical models of disks (Gorti & Hollenbach 2008; Kamp et al. 2011) predict much higher line fluxes than what we observe for our disk sources, even after accounting for calibration uncertainties (our flux estimates are predicted to be $\sim 30\%$ low, see Section 3.2.3), suggesting that the [O I] emission is still not fully understood. Outflow sources have much stronger line fluxes than their disk-only counterparts, with values that can be up to 20 times stronger for the same continuum flux compared to a non-outflow source. Therefore an outflow, if present, can dominate the line emission, especially for strong outflows. This is discussed further in Section 4.5.

5.2. What Can We Learn from the [O I] 63/145 Line Ratios?

If the emission of [O I] $145\ \mu\text{m}$ and [O I] $63\ \mu\text{m}$ came from the same region, our observed line ratios 10–25, would suggest optically thin emission originating from gas with a temperature of a few 100 K (Tielens & Hollenbach 1985) located at the inner part and surface layers of the disk or from the shock regions in the outflow. However, we would also see similar ratios for optically thick lines, if the [O I] $145\ \mu\text{m}$ line, which requires hotter gas, came from a more compact source (like only the inner part of the disk).

Disk sources (DE Tau is an exception) and transitional disks do not show either [O I] $145\ \mu\text{m}$ or [C II] $158\ \mu\text{m}$, because these disks are intrinsically faint and the emission is below our detection limit.

Kamp et al. (2011) explored the [O I] 63/145 line ratios using the results from the DENT grid (Disk Evolution with Neat Theory) that consists of 300,000 disk models with 11 free parameters. They find that the median of the [O I] 63/145 line

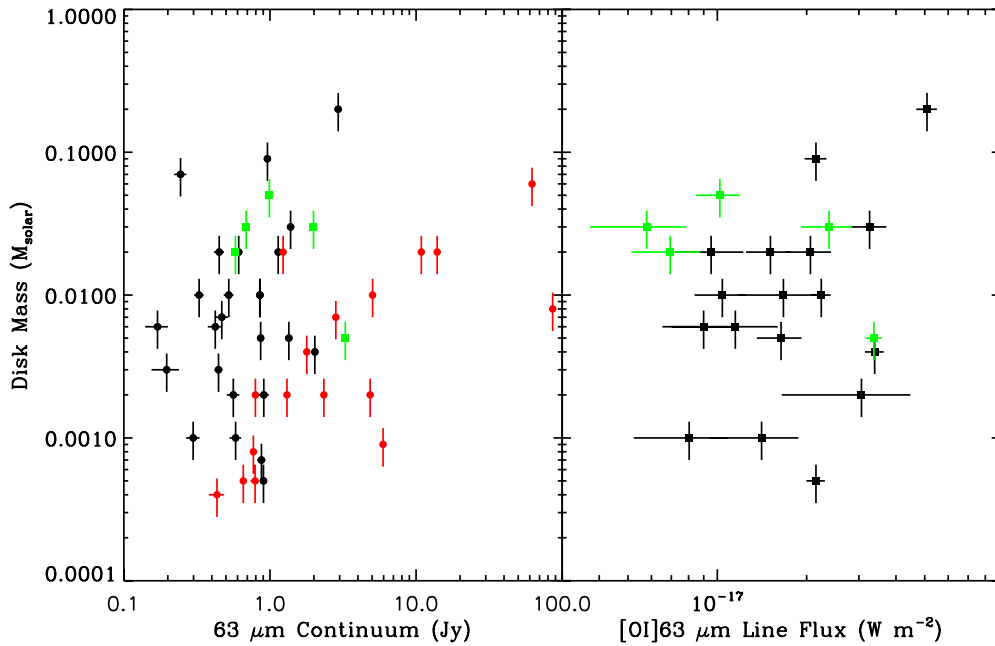


Figure 7. Disk mass estimates from Andrews & Williams (2005) as a function of [O I] 63 μm line flux and 63 μm spectroscopic continuum flux (right panel) and the 63 μm continuum (left panel). Detections of $\lesssim 3\sigma$ in either continuum or line flux are omitted. Red points are targets with known outflow activity, black points are sources with no known outflow, and green points represent known transitional disk sources. Known outflow sources have been omitted from line flux plot, as our analysis show that when a star drives an outflow, the outflow dominates the [O I] 63 μm emission. There is no correlation between disk mass and [O I] 63 μm line emission nor with the 63 μm continuum flux.

(A color version of this figure is available in the online journal.)

ratios for the whole DENT grid is 25, while the ratio is ~ 16 for the canonical gas-to-dust ratio of 100. Similar ratios are found for the disk models by Meijerink et al. (2008), who found that [O I] 145 μm line emission is 20–40 times fainter than the [O I] 63 μm line. This also agrees with the results by Meeus et al. (2012), who studied a sample of isolated HAEBE stars. They found that when the [O I] 145 μm line was detected, it was typically 20–30 times fainter than the [O I] 63 μm line. For such line ratios we would not expect to detect the [O I] 145 μm line in any of our “disk-only” sources. Line ratios of 10–50 are also predicted by shock models (Hollenbach & McKee 1989; Flower & Pineaut des Fôrets 2010). Thus the [O I] 63/145 line ratios does not help us to discriminate between a jet or a disk origin.

Liseau et al. (2006), who analyzed all *ISO-LWS* observations of young objects with outflows (mostly Class I and Class 0 objects), found surprisingly low [O I] 63 μm to [O I] 145 μm ratios; more than half of their sample had line ratios less than 10. The average line ratio of the ones that had a line ratio less than 10 was 5.3 ± 2.6 . Even though our sample consists mostly of Class II sources, we do include some Class I sources and several of our Class II sources drive powerful outflows. We would therefore have expected to see some low ratios, especially since all the sources detected in [O I] 145 μm are outflow sources, but we do not. Essentially all of our detections have a ratio $\gtrsim 10$, see Figure 5. A recent paper from the guaranteed time Key program WISH (Karska et al. 2013) discuss PACS observations of [O I] in 18 low-mass protostars, 5 of which were Class I and the rest were Class 0 sources. They also find much higher line ratios than Liseau et al. (2006). In their Class 0 sample Karska et al. found the [O I] 63 μm to [O I] 145 μm line ratios to vary from 5.5 to >45 , with a median of ~ 10.4 , while their Class I samples varies from 10.4 to 26.5. Overall there does not seem to be much of a difference between the results obtained by Karska et al. and us. Their Class 0 sample has somewhat smaller ratios but the ratios for the Class I sources are about the same as we find in

Taurus. The most likely explanation for the lower ratios found by Liseau et al. is probably due to calibration. The difference in beam size should have a rather minor effect, since the [O I] emission is rather compact, and if anything one would expect the 63 μm line to be spatially more extended than the 145 μm line, which would push the ratio to higher values, not lower ones.

5.3. Disk Mass versus [O I] 63 μm Line Emission

Kamp et al. (2010) suggested that the [O I] 63 μm and the [C II] 158 μm lines, especially when combined with CO, may provide a tool to measure the disk gas mass (see also, Kamp et al. 2011). Our observations, however, show that even with *Herschel* we do not have the sensitivity to detect [C II] in disks around low-mass stars; all our [C II] detections are outflow sources and the line emission, when detected, is almost certainly from shock or PDR emission in the outflow (Podio et al. 2012). On the other hand, [O I] 63 μm , as shown in the previous section, clearly originates in the disk, because we detected the line in 20 stars, which show little or no outflow activity. There are not enough observations of any given CO transition to enable a meaningful investigation of how the [O I]/CO ratio correlates with disk mass. However, if the [O I] 63 μm emission probes the disk gas mass, one might expect some sort of correlation between [O I] line flux and total disk mass.

After searching through the literature, we decided to use the disk mass estimates for the large sample investigated by Andrews & Williams (2005). A homogeneous treatment is more important than accuracy for this investigation, because published mass estimates vary greatly depending on how they have been estimated, and what dust emissivities have been used (see, e.g., Ricci et al. 2010, 2012; Guilloteau et al. 2011). As we can see from the right panel in Figure 7, there is no correlation between [O I] 63 μm line flux and disk mass. We increased our sample by plotting the disk mass as a function of 63 μm

continuum flux density, since the continuum emission originates in the disk and is not affected by the outflow. However, as we can see from the left panel in Figure 7, where we plotted outflow sources in red, they also reveal no correlation and the same is true for the whole sample. For the same $63\ \mu\text{m}$ continuum flux density or line intensity the disk mass can vary by more than a factor of 100.

5.4. Source of $63\ \mu\text{m}$ Continuum Emission

Why is there a correlation between $[\text{O I}]$ $63\ \mu\text{m}$ and the $63\ \mu\text{m}$ continuum? The simplest explanation for the tight correlation is that both line and continuum emission come from the same region of the disk. In order to investigate where the $63\ \mu\text{m}$ continuum emission originates in the disk, we first investigated the simple disk model used by Andrews & Williams (2007), which uses the broadband SEDs and sub-millimeter visibilities to constrain some of the basic parameters that describe the structure of the disk. Using their flat disk model (as described in Andrews & Williams 2007), we find that for the majority of their sources that are also in our Taurus sample, 90% of the $63\ \mu\text{m}$ continuum emission comes from the inner $\sim 10\%$, or $\sim 5\text{--}50$ AU, depending on the size of the disk. It should be noted, however, that overall disk size is poorly constrained in these models. Models of T Tauri stars with MFOST (Pinte et al. 2006), which include disk flaring, give similar results. For the Class II objects in our Taurus sample, it therefore appears that a significant fraction of the line emission also originates in the inner part of the disk.

As a next step we explored the bulk properties of the disks using isothermal two-component graybody models. For these fits we use all published millimeter and sub-millimeter continuum fluxes combined with the far-infrared fluxes from this paper. To constrain the warm dust in the disk we also included MIPS $24\ \mu\text{m}$ and/or WISE $22\ \mu\text{m}$ data from the WISE All-Sky survey. The MIPS $24\ \mu\text{m}$ data are taken from (Luhman et al. 2010) and/or Rebull et al. (2010); the latter also includes MIPS $70\ \mu\text{m}$ data. The $22\ \mu\text{m}$ and $24\ \mu\text{m}$ mid-IR flux densities are still completely dominated by dust emission from the disk for the Taurus Class II sources and the contribution from the photospheric emission is negligible. The fitting program allows us to put in constraints for the dust temperature, and fits separately the size of both the cold and the warm dust as well as the dust emissivity index. In order to limit the number of fitted parameters we do not fit the dust emissivity index, β , of the warm component; instead we set it to 1. Whether we use $\beta = 1.0$ or 1.5 does not really matter, the dust temperature is essentially the same to within a degree. The results of these fits for a sample of 21 sources (both disk and outflow sources, but not transitional disks), for which we had sufficient data, indicate that the temperature of the warm dust ranges from ~ 95 K to 190 K, with a median of 130 K. This is about the temperature we would expect for the $[\text{O I}]$ emitting gas (U. Gorti 2012, private communication). There is no difference in the temperature of the warm dust between outflow sources and non-outflow sources. Figure 8 presents several examples of these graybody fits. These results suggest that the $[\text{O I}]$ emission originates in regions where the gas and dust are approximately thermalized. This might be the inner part of the disk or the warm, lower surface layers of the disk.

As we saw earlier, we also see a correlation between $[\text{O I}]$ $63\ \mu\text{m}$ flux and continuum emission in the transitional disks, but the $[\text{O I}]$ emission is consistently weaker by a factor of two or more for the same continuum flux. Two component

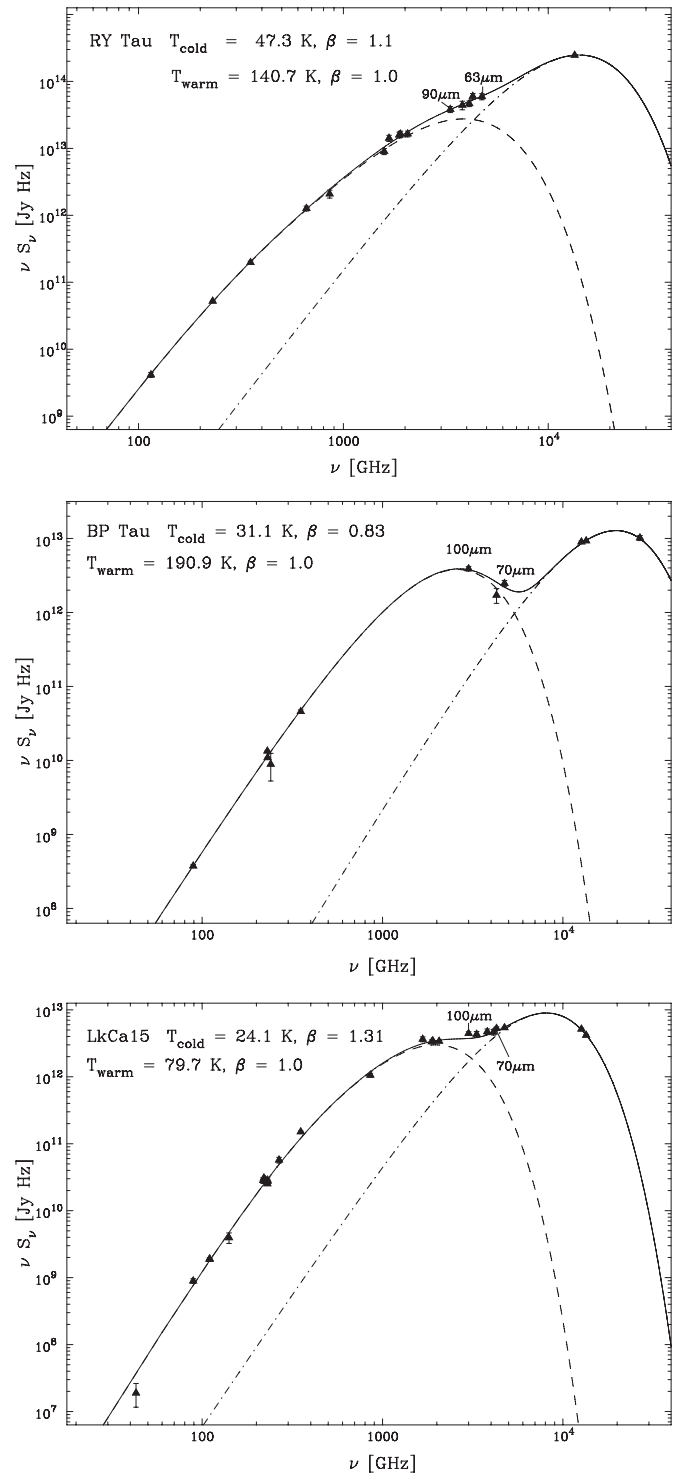


Figure 8. Representative two component graybody fits. Millimeter and sub-millimeter data come from literature, far-infrared data from this paper, MIPS $24\ \mu\text{m}$ and/or $70\ \mu\text{m}$ fluxes are also from literature, while WISE $22\ \mu\text{m}$ fluxes are from the WISE All-Sky Catalog. Since we do not include photometry shortward of $12\ \mu\text{m}$, we can ignore the hot inner disk and the stellar photosphere.

graybody fits of these transitional disks yield substantially cooler temperatures for the warm dust, i.e., the dust dominating the $63\ \mu\text{m}$ continuum emission. For this sample the warm dust covers a relatively narrow temperature range, about $80\text{--}90$ K, with a median of 85 K. This is consistent with the lower observed $[\text{O I}]$ $63\ \mu\text{m}$ line emission in these transitional disks. If the dust and gas is coupled in $[\text{O I}]$ emitting regions of the disk, the

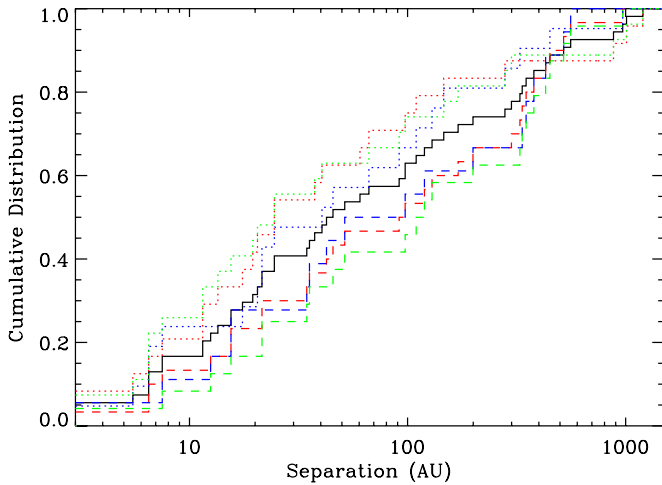


Figure 9. Cumulative distribution of separations for binaries systems in our sample. The black histogram represents all multiple systems in our survey. Dashed and dotted histograms represent subsamples of object which are respectively detected and non-detected in $70\ \mu\text{m}$ (red) and $850\ \mu\text{m}$ (green) continuum and $[\text{O I}] 63\ \mu\text{m}$ (blue). Tight binaries (below ~ 50 AU) are more likely to be undetected in all three types of observations than wider systems. (A color version of this figure is available in the online journal.)

lower temperature compared to “normal” Class II disks readily explains the lower line intensity. We note, however, that this interpretation may be oversimplified. More detailed modeling of transition disks will be presented in a forthcoming paper (F. Ménard et al. 2013, in preparation) showing that lowering the dust temperature alone makes the line too low (i.e., does not change the ratio properly) and that direct illumination of the disk rim probably needs to be taken carefully into account as well.

5.5. Multiplicity

The presence of stellar companions has potentially dramatic consequences on the properties of circumstellar disks through the tidal forces exerted on them. For instance, it has been established that T Tauri stars in close binaries ($\lesssim 50$ AU) are much less likely to host disks (Cieza et al. 2009; Kraus et al. 2012). Furthermore, there is evidence that disks in these systems are much less massive than those in wider binaries or around single stars (Harris et al. 2012, but see Duchêne 2010). It is thus natural to explore the connection between multiplicity and our continuum and line observations. In particular, our survey allows one to address this question for the gaseous component of protoplanetary disks. To this end, we have compiled the multiplicity properties of each system in our sample (Kenyon et al. 2008; Kraus et al. 2011; R. J. White et al. 2013, in preparation). For high-order multiple systems, we first evaluated which component hosts the disk dominating the far-infrared emission, typically from high-resolution sub-millimeter mapping (e.g., Harris et al. 2012), and assigned the separation of the system to the closest companion around that component but excluding spectroscopic companions.

The detection rate of multiple systems is lower than that of single stars for both continuum and line emission. The continuum detection rate is 32/56 for binaries and 36/55 for singles with a significance level of 90%. The line detection rate is 20/41 for binaries and 23/34 for singles with a significance level of 95%. Not surprisingly, we find that systems tighter than 50–100 AU are less likely to be detected at far-infrared continuum or $[\text{O I}] 63\ \mu\text{m}$ emission than wider systems (Figure 9),

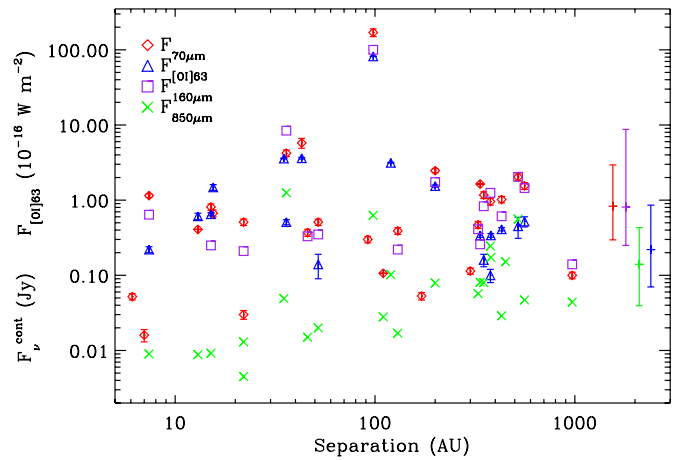


Figure 10. Far-infrared and sub-millimeter continuum and line fluxes for all multiple systems in our sample as a function of the system’s (projected) separation. For high-order multiple systems, we assigned to the system the separation to the closest companion to the disk-bearing component of the system to the exclusion of spectroscopic companions. We plot here the continuum fluxes at $70\ \mu\text{m}$ (PACS, red diamonds), $160\ \mu\text{m}$ (PACS, purple squares), and $850\ \mu\text{m}$ (Andrews & Williams 2005, green crosses), and the $[\text{O I}] 63\ \mu\text{m}$ line flux (PACS, blue triangles). Uncertainties displayed on PACS datapoint do not include calibration uncertainties, whereas a typical uncertainty of 10%–20% applies to all sub-millimeter points. Notice how binaries tighter than 50–100 AU have systematically reduced sub-millimeter fluxes whereas their far-infrared continuum and line fluxes span the same range as those of wider systems. The “error bars” on the right-hand side of the plot show the median and the 34 percentile on each side (e.g., 1σ range) for single stars in our sample.

(A color version of this figure is available in the online journal.)

similar to conclusions reached from near- and mid-infrared as well as sub-millimeter wavelengths. Taken at face value, this suggests that the gas and dust components of disks are similarly affected by the presence of a companion. We note, however, that the detailed interpretation of these conclusions is complicated by the biased nature of the GASPS sample, which over-represents disk-bearing systems, especially for spectroscopic observations. Nonetheless, an intriguing finding is that neither the $70\ \mu\text{m}$ nor the $[\text{O I}] 63\ \mu\text{m}$ line flux show a correlation with the binary separation in systems for which they are detected (Figure 10). This is opposite the results of sub-millimeter surveys (e.g., Harris et al. 2012) but in line with near- and mid-infrared studies (Cieza et al. 2009), further suggesting that both the continuum and line emission arise from the inner most regions of the disk, which are not truncated by stellar companions located 10 AU or more from the disk-bearing star.

5.6. Class III Objects (Weak-line T Tauri Stars)

We do not detect line emission in any of the 15 WTTSs, which we observed in $[\text{O I}] 63\ \mu\text{m}$ (Table 2). In continuum we observed 44 Class III objects and detected only three of them: FW Tau, V397 Aur, and V819 Tau. All three have $70\ \mu\text{m}$ flux densities far below our $[\text{O I}] 63\ \mu\text{m}$ detection threshold, if they follow the correlation found for “disk-only” sources, and would therefore require unrealistically long integration times to reach the expected signal level we predict from CTTS. V819 Tau (spectral type K7) was classified as Class II by Luhman et al. (2010) and Class III by Rebull et al. (2010). It was detected at $70\ \mu\text{m}$ by Cieza et al. (2013), who did detailed SED modeling showing that the star has no excess in the IRAC bands but a clear excess at $24\ \mu\text{m}$ and $70\ \mu\text{m}$. Their modeling suggests that V819 Tau has a warm debris disk. We detected V819 Tau at both $70\ \mu\text{m}$ and $100\ \mu\text{m}$, because we have longer exposure times than

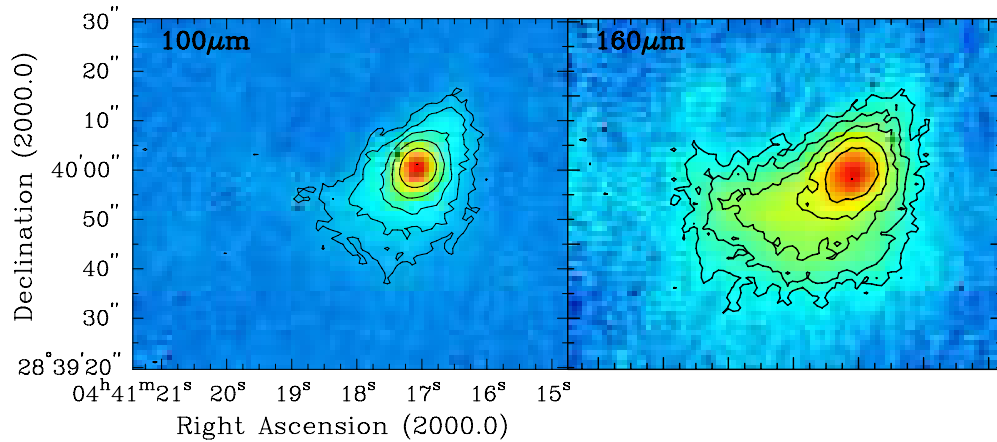


Figure 11. False color images of CoKu Tau/4 overlaid with logarithmic contours. CoKu Tau/4 is surrounded by an extensive far-infrared nebosity at 160 μm , which is much fainter at 100 μm .

(A color version of this figure is available in the online journal.)

Cieza et al. We see no trace of emission at 160 μm . Both FW Tau and V397 Tau were detected in all bands observed. Whether these disks are at the end of their primordial phase or whether the stars have already reached the debris disk stage is impossible to judge without detailed modeling.

5.7. Comments on Individual Objects

Here we highlight a few stars, which previously were not known to power jets or which appear to have unusual characteristics.

AA Tau, spectral type K7–M0 V, is a well-studied CTTS, which has long been believed to power an optical jet (Hirth et al. 1997; Bouvier et al. 1999, 2003, 2007). This was recently confirmed by Cox et al. (2013) who found a poorly collimated, faint jet extending to 21'' from the star. The [O I] $\lambda 6300$ line in AA Tau is narrow and slightly blue-shifted (Hirth et al. 1997; Hartigan et al. 1995). The He I $\lambda 10830$ line is likewise faint, narrow and slightly blue-shifted (Edwards et al. 2006), whereas it is expected to be deep, broad and blue-shifted for an outflow source (cf. discussion on DL Tau below).

Baldovin-Saveedra et al. (2011) searched for mid-IR emission lines in a sample of 64 PMS stars in Taurus and detected [Ne II] 12.81 μm emission in 18 objects including AA Tau. They found in general that the luminosity of the [Ne II] line was stronger for sources driving jets than that for those without known jets, although not for AA Tau. Najita et al. (2009), who analyzed high-resolution [Ne II] emission line profiles from AA Tau found that they could be explained by originating in the disk, although they could not rule out contribution from a jet. Our [O I] 63 μm observations, however, show that [O I] line is consistent with a disk origin (Figure 6), i.e., with little or no excess emission from the jet. However, since it has been shown to drive a faint jet, we classify it as a jet/outflow source. The inner disk of AA Tau is rich in organic molecules (Carr & Najita 2008). The o-H₂O line at 63.32 μm has also been detected for this source (Riviere-Marichalar et al. 2012).

CoKu Tau/4 is a M1.5 T Tauri star with weak H α emission (Cohen & Kuhl 1979; Kenyon et al. 1998) and it therefore has a low accretion rate. It was identified by Forrest et al. (2004) as a transitional disk based on *Spitzer*/IRS observations, which revealed that it has no infrared excess shortward of 8 μm , but a large excess at 20–30 μm indicating that the region within 10 AU have been largely cleared of dust. Ireland & Kraus (2008)

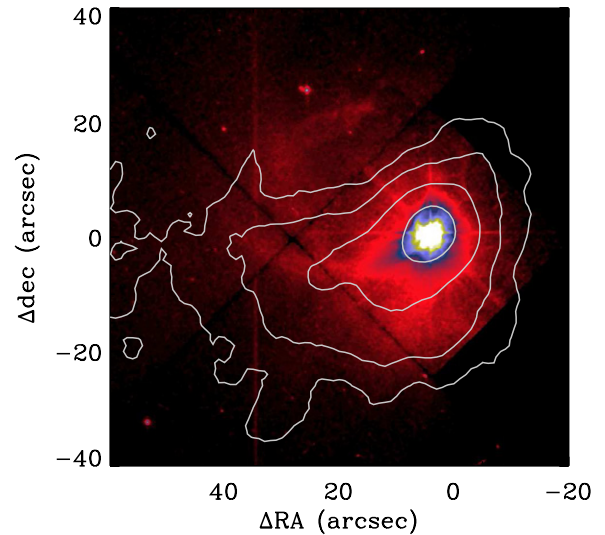


Figure 12. WFPC 2 image (0.8 μm) of the reflection nebosity illuminated by CoKu Tau/4. The PACS 160 μm image (contours) closely follows the nebosity.

(A color version of this figure is available in the online journal.)

carried out aperture-masking interferometry and adaptive optics imaging of the star and show that CoKu Tau/4 is a near-equal binary star of projected separation ~ 8 AU (53 mas). The binary has therefore cleared the inner disk. Both stars are of spectral type M1–M2 and are ~ 3 –4 Myr old (Ireland & Kraus 2008). It is therefore not a transitional disk.

CoKu Tau/4 is a strong far-infrared source (Table 1) and one of the few stars in our sample which is associated with a far-infrared nebosity (Figure 11). At 70 μm the star appears point-like, but at 100 μm nebosity can be seen to the south and southeast of the star. At 160 μm the emission extends over more than an arcminute (Figure 11). The far-infrared nebosity follows closely the reflection nebosity seen with WFPC 2 camera on the *Hubble Space Telescope*²² (Figure 12). The [O I] flux is consistent with a disk origin (Figure 6).

DE Tau is a young CTTS of spectral type M2 (Kenyon & Hartmann 1995). It is not known to drive an outflow. It stands out

²² The WFPC 2 image for CoKu Tau 4 was obtained as part of *HST* program GO 9160; PI: D. L. Padgett.

in our sample as the only non-outflow star with a 3σ detection of the [O I] $145\ \mu\text{m}$ line and only a marginal ($\sim 2\sigma$) detection of the [O I] $63\ \mu\text{m}$ line. For DE Tau the upper limit of the line ratio of [O I] 63 to [O I] $145\ \mu\text{m}$ is on the order of unity, suggesting that both transitions are optically thick and originate from the same part of the disk. An isothermal graybody fit to the millimeter and far-infrared SED requires the dust to be optically thick at millimeter wavelengths, i.e., a dust emissivity index of 0, suggesting that DE Tau could be surrounded by a compact optically thick disk.

DG Tau and DG Tau B both power optical jets (Mundt & Fried 1983; Mundt et al. 1987; Kepner et al. 1993; Eisloffel & Mundt 1998). DG Tau is a young, heavily accreting star with a spectral type of K7–M0 (Gullbring et al. 1998), obscured by a visual extinction of 3.2–5.4 mag (Fischer et al. 2011). It also powers a low velocity, wide-angled bipolar molecular outflow (G. Sandell, 2013, private communication). The disk has been imaged with high spatial resolution at millimeter wavelengths and is seen relatively face on with an inclination of $\sim 30^\circ$ (Isella et al. 2010; Guilloteau et al. 2011). In this case we find the [O I] $63\ \mu\text{m}$ emission to be completely dominated by the outflow but only marginally extended. Podio et al. (2013) spectrally resolved the [C II] $158\ \mu\text{m}$ line with HIFI, which shows that the [C II] emission originates in the blue-shifted jet, and not in the disk.

DG Tau B is a deeply embedded Class I source. The spectral type is unknown, but modeling of the SED suggests that it is low mass ($\leq 0.3\ M_\odot$), i.e., mid M. It powers a well-collimated bipolar molecular outflow (Mitchell et al. 1997). Compared to DG Tau the [O I] $63\ \mu\text{m}$ emission is clearly extended and much stronger in the red-shifted outflow lobe than on the star (Podio et al. 2012). At $70\ \mu\text{m}$ the continuum emission is unresolved on both stars, but at $100\ \mu\text{m}$ and especially $160\ \mu\text{m}$ one can see faint emission from the surrounding dark cloud, possibly from dust being heated and compressed by the outflows that are powered by DG Tau and DG Tau B. The PACS line spectroscopy from both stars is discussed in detail by Podio et al. (2012).

DL Tau, a CTTS of spectral type K7 V, is classified as an outflow/jet source based only on the broad [O I] $\lambda 6300$ and [S II] $\lambda 6371$ (Hartigan et al. 1995). The [O I] $\lambda 6300$ line shows a high velocity component, which is blue-shifted to $\sim -300\ \text{km s}^{-1}$, while the [S II] $\lambda 6371$ goes to $-250\ \text{km s}^{-1}$, and has no low velocity component at all. DL Tau has deep and broad blue-shifted He I $\lambda 10830$ (Edwards et al. 2003, 2006), which Kwan & Fischer (2011) show originates in an outflow rather than from accretion. C. Grady (2013, private communication) reports that a jet as well as two distant HH objects have recently been discovered in DL Tau. The disk is seen relatively face-on with an inclination $i = 38 \pm 2^\circ$ (Guilloteau et al. 2011). We find the [O I] $\lambda 63\ \mu\text{m}$ emission to be in the outflow regime (Figure 6), which confirms that DL Tau indeed powers an outflow.

GG Tau is a hierarchical quadruple system with a $10''$ separation between the two binaries (Leinert et al. 1991). GG Tau was one of the brightest millimeter sources in the survey by Beckwith et al. (1990) suggesting that it must be surrounded by a massive circumstellar disk. Millimeter interferometry (Simon & Guilloteau 1992; Guilloteau et al. 1999) shows that GG Tau Aa/Ab is surrounded by a large circumbinary disk with an outer radius of $2''$ – $4''$. GG Tau Aa has a spectral type of K7, while the secondary, GG Tau Ab, has a spectral type of M0.5 (White et al. 1999). The inner part of the ring/disk has been resolved in high-resolution scattered light images from 0.5 to $4\ \mu\text{m}$ (Roddier et al. 1996; McCabe et al. 2002; Duchêne et al. 2004; Krist

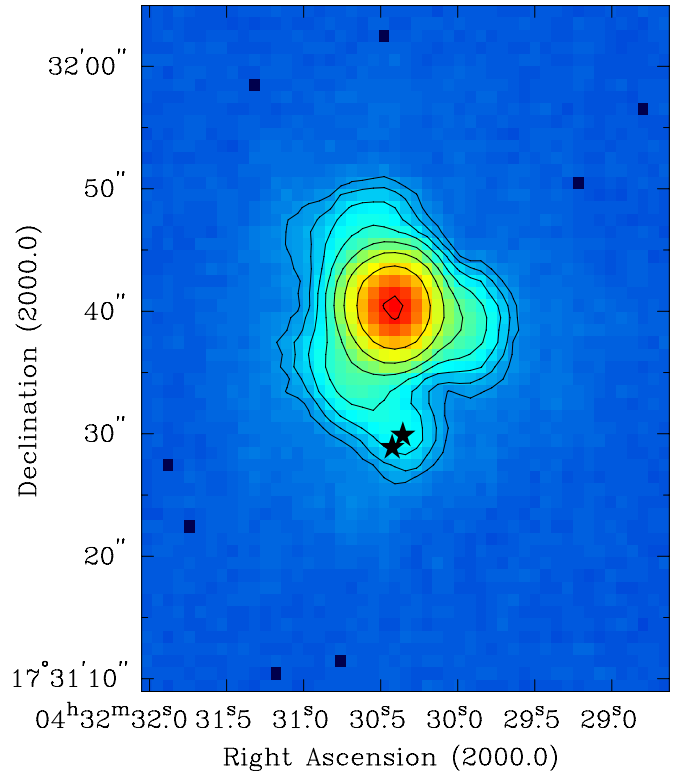


Figure 13. Logarithmically stretched $70\ \mu\text{m}$ image of GG Tau showing the trifoil structure of the PSF. The additional spur to the south coincides with the southern binary, GG Tau Bab, which is shown with star symbols. A PSF subtraction (not shown) confirms the detection of GG Tau B.

(A color version of this figure is available in the online journal.)

et al. 2005) and found to be elliptical with a semimajor axis of $1''.5$.

The secondary pair, GG Tau Ba and Bb is also a binary and separated from the primary by $10''.4$ at a P.A. of 185° (Kraus & Hillenbrand 2009). GG Tau Ba has a spectral type of M5 and Bb M7 (White et al. 1999). We detect faint emission from the system at $70\ \mu\text{m}$ (Figure 13).

HV Tau and DO Tau are two CTTSs associated with far-infrared nebulosities. The separation between the two is $\sim 90''.8$ and both were imaged simultaneously with the PACS imager, although DO Tau is close to the edge of the image. Both stars are associated with far-infrared nebulosities, which become visible at $100\ \mu\text{m}$ (Figure 14). At $160\ \mu\text{m}$ the emission is very extended and connect both stars in a common envelope.

DO Tau is a G star associated with an arc-like nebula, which is aligned with the nebulosity we see at 100 and $160\ \mu\text{m}$ (McGroarty & Ray 2004). It drives a bipolar jet with the redshifted jet at a P.A. of 70° (Hirth et al. 1994), approximately aligned with the arc-like nebulosity we see at $100\ \mu\text{m}$. McGroarty & Ray (2004) found three HH objects at P.A.s of 74° – 78° northeast of DO Tau. The farthest one, HH 831 B, is $11'$ from DO Tau.

HV Tau is a close binary (Simon et al. 1996), which show no infrared excess (Woitak & Leinert 1998). About $4''$ to the northeast is a third star, HV Tau C, which has an edge on disk (Monin & Bouvier 2000; Terada et al. 2007). The spectral type of HV Tau C is K6 (White & Hillenbrand 2004). This is the star we see in the far-infrared, and which powers a bipolar jet (Stapelfeldt et al. 2003; McGroarty & Ray 2004; Duchêne et al. 2010) with the P.A. of the blue-shifted jet being

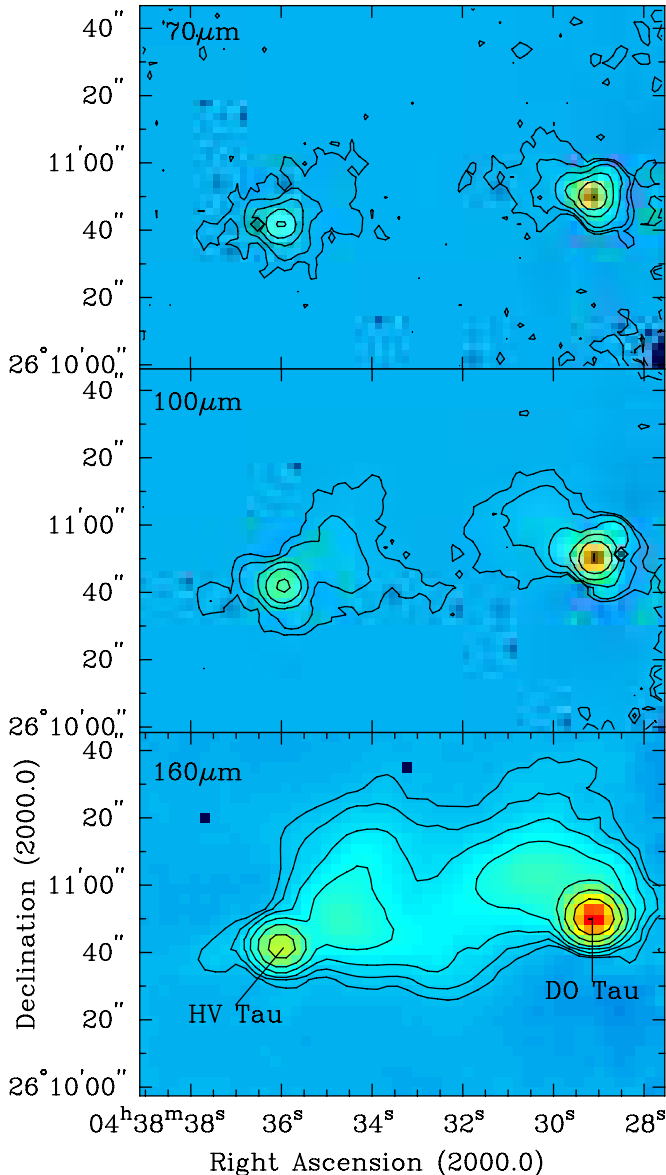


Figure 14. False color images of HV Tau and DO Tau at $70\ \mu\text{m}$, $100\ \mu\text{m}$, and $160\ \mu\text{m}$ overlaid with logarithmic contours. DO Tau is close to the edge of the image, which results in excess noise east of the star. Both stars appear to be associated with extended emission, which is barely visible at $70\ \mu\text{m}$. At $160\ \mu\text{m}$ the emission is very extended.

(A color version of this figure is available in the online journal.)

$\sim 25^\circ$ (McGroarty & Ray 2004). In this case the V-shaped $100\ \mu\text{m}$ emission is aligned with a diffuse reflection nebula west-northwest of the star (Martín et al. 1994), which appears to be approximately aligned with the disk plane, and orthogonal to the jet.

We find that both stars have strong $[\text{O I}] 63\ \mu\text{m}$ emission, as expected from stars powering jets.

HL Tau and XZ Tau are two of the first T Tauri stars found to power well-collimated optical jets (Mundt & Fried 1983; Mundt et al. 1990; Movsessian et al. 2007). HL Tau is a Class I object of spectral type K7 (White & Ghez 2001). It has very strong high velocity blue-shifted $[\text{O I}] \lambda 6300$ emission (Edwards et al. 1987) and it is one of the brightest T Tauri stars at 1.3 mm (Beckwith et al. 1990). The disk has an inclination angle of $\sim 42^\circ$ (Lay et al. 1997). The $[\text{O I}] 63\ \mu\text{m}$ emission is definitely in

the outflow regime (Figure 6), but it does not have a particularly strong excess. XZ Tau, which has a lower accretion rate, has a much larger excess in $[\text{O I}] 63\ \mu\text{m}$ due to the outflow.

RY Tau is classified as a F8–G1 type star (Mora et al. 2001; Calvet et al. 2004), although Kenyon & Hartmann (1995) assigned it a spectral type as late as K1. It is a well known outflow source, which drives a well-collimated jet extending out at least $31''$ from the star and with a counter-jet extending out to at least 3.5 in the opposite direction (St-Onge & Bastien 2008). The star has relatively strong free-free emission (Rodmann et al. 2006), which is consistent with a thermal wind. The spectro-imaging observations by Agra-Amboage et al. (2009) detect the blue-shifted $[\text{O I}] \lambda 6300$ within $2''$ of the star, consistent with the large scale jet seen by St-Onge & Bastien (2008). Agra-Amboage et al. (2009) estimate the inclination of the jet to be between 45° – 77° . Isella et al. (2010) resolved RY Tau at 1.3 mm with millimeter interferometry and found that it has a large central cavity (28 AU) similar to what is seen in transitional disks. Alternatively the dust grains in the inner disk have grown to centimeter sizes lowering the dust opacity. Espaillat et al. (2011) found that they could fit the SED of RY Tau with an 18 AU gap which contains some optically thin dust consistent with the cavity observed by Isella et al. (2010).

RY Tau is also peculiar in other respects. Lommen et al. (2010) find a correlation between the strength of the $10\ \mu\text{m}$ silicate feature and the slope of the millimeter emission measured between 3 and 1 mm, except for RY Tau, which in their data set is an extreme outlier, although this is not entirely true. Our analysis, based on all published millimeter/sub-millimeter data, shows that the millimeter slope is rather normal, therefore in that respect RY Tau is not that unusual. The strong silicate emission, however, requires an abundance of small grains. What is unique though is that a transitional disk star would drive a well-collimated optical jet, have free-free emission and still be rather strongly accreting ($\dot{M} \sim 6\text{--}9 \times 10^{-8} M_\odot \text{ yr}^{-1}$; Agra-Amboage et al. 2009).

Our observations shows no excess from the jet in the $[\text{O I}] 63\ \mu\text{m}$ line. The line intensity is completely consistent with a disk origin (Figure 6). This could mean either that there is no $[\text{O I}] 63\ \mu\text{m}$ emission from the outflow or that the emission from the disk is anomalously low, perhaps due to the central cavity.

StHA 34 (HBC 425) is a spectroscopic binary with components of nearly equal luminosity and temperature (both M3) and broad, strong $\text{H}\alpha$ emission characteristic of a CTTS (White & Hillenbrand 2005). However, neither component of the binary shows $\text{Li I } \lambda 6708$ absorption suggesting a very long-lived accretion disk. Comparison with PMS evolutionary models give an isochronal age of 8 ± 3 Myr, which is much younger than the predicted lithium-depletion timescale of ~ 25 Myr. Hartmann et al. (2005), who observed StHA 34 with IRS on *Spitzer* modeled the infrared SED with three components: an inner disk wall, an optically thin inner disk, and an outer disk, i.e., similar to the SED of a transitional disk. They favored an age of 25 Myr, which would require StHA34 to be at a distance of ~ 100 pc, and therefore not a member of the Taurus association.

Dahm & Lyke (2011) found a low-mass companion $\sim 1''.23$ southeast of the primary pair, which has strong $\text{Li I } \lambda 6708$ absorption. StHA 34 C has a spectral type of M5.5. Comparison with PMS evolutionary tracks imply a mass of $\sim 0.09 M_\odot$ and an age of 8–10 Myr assuming the nominal distance to Taurus (140 pc). It therefore seems more likely that StHA 34 is lithium depleted and not surrounded with a 25 Myr old, still accreting circumbinary disk.

We detected StHA 34 in continuum at 70, 100, and 160 μm (Table 1). The emission is rather faint, which is consistent with an evolved, possibly transitional disk.

T Tauri is an exceptional member of the class of PMS stars that share its name. It is a hierarchical triple system with the optical star T Tau N having a K-type spectrum and large optical variations on timescales of months to years (Beck & Simon 2001), and the southern deeply embedded binary system T Tau S, which has a projected separation of $0''.05$ (Koresko 2000). T Tau N is known to power a bright optical jet (Bührke et al. 1986). T Tau S is surrounded by a massive accretion disk and powers a spectacular jet (Reipurth et al. 1997).

ISO found T Tauri to have the richest line mid/FIR emission line spectrum of any PMS star (Lorenzetti 2005). T Tauri is very bright in the far-infrared (Table 2), and the emission is extended ($\sim 4''$) in all PACS bands. We see faint emission from the Hind’s nebula at 70 μm , which is much stronger at 100 and 160 μm . At 160 μm we also start to pick up emission from the surrounding cloud.

Since T Tauri is a triple system which drives at least two optical jets, it is not clear where the emission originates. It could arise in the disk, in the outflow, or in the hot surrounding envelope (Podio et al. 2012). We have therefore excluded it from any correlation analysis.

V773 Tau is a compact quadruple system with at least four stars within $0''.3$ (Boden et al. 2012). V773 Tau A is a spectroscopic binary with spectral types of K2 and K5 (Wely 1995). It is a WTTS and one of the strongest radio stars in Taurus (O’Neal et al. 1990; Massi et al. 2008). The radio emission is non-thermal and strongly variable (Dutrey et al. 1996). The variability is due to interacting coronae, which causes strong flaring at periastron (Massi et al. 2008). V773 Tau A has no near infrared excess, and is therefore unlikely to be surrounded by a circumbinary disk. V773 Tau B is a CTTS, which varies by more than 0.5 mag in the visible and has a spectral type of K7–M0.5 (White & Ghez 2001; Duchêne et al. 2003; Boden et al. 2012). It has some near-IR excess longward of 2 μm and maybe surrounded by a compact disk. V773 Tau C is extremely red and almost certainly surrounded by a circumstellar disk (Duchêne et al. 2003). Since V773 Tau was detected at 1.3 mm and 850 μm (Osterloh & Beckwith 1995; Andrews & Williams 2005) it is clear that the system must have a circumstellar disk. Furthermore we easily detected it at both 60 and 160 μm (Table 2). Whether the dust emission is dominated by V773 Tau C or whether V773 Tau B also contributes requires observations with sub-arcsecond imaging resolution with good sensitivity, as can be provided by ALMA.

V773 Tau is not known to drive a jet, yet the [O I] 63 μm flux density clearly puts it in the outflow regime (Figure 6). Cabrit et al. (1990) did detect [O I] $\lambda 6300$ and [S II] $\lambda 6731$ emission but did not publish a spectrum. It is not clear whether the emission comes from a jet, especially since the velocity offsets were small. However, FM Tau, an M0 star, is $38''$ to the north–northwest of V773 Tau, and CW Tau, a K3 star, $92''$ to southeast. The latter is a young Class II type CTTS, which powers a bipolar optical jet and excites several HH objects (Dougados et al. 2000; McGroarty & Ray 2004). Not all the HH objects discovered by McGroarty & Ray (2004) can be explained by the outflow from CW Tau. In particular, HH 828, which is just north of FM Tau and V773 Tau, is not aligned with the CW Tau jet, and therefore more likely to be powered either by FM Tau or V773 Tau. The [O I] $\lambda 6300$ line in FM Tau is slightly blue-shifted and does not show much high velocity emission (Hartigan et al. 1995), and

is therefore an unlikely source. V773 Tau may well be exciting HH 828. In our analysis we therefore assume that V773 Tau is an outflow source, although this still needs to be confirmed.

6. SUMMARY AND CONCLUSIONS

In this paper we present the results of *Herschel*/PACS photometric and spectroscopic observations of a large sample of T Tauri stars in the Taurus/Auriga star-forming regions as part of the GASPS survey. We observed 82 fields in photometry and 75 in spectroscopy, for a total sample of about 120 objects, mostly Class II/III objects (CTTS/WTTS) as well as a handful of embedded Class I sources and transitional disks.

In photometry, we detected 50 known members of the association, apart for 3 Class III sources (FW Tau, StHA 34, and V819 Tau), all of them are Class II or Class I sources. Most objects are spatially unresolved in the continuum. Exceptions include T Tau, the multiple systems UZ Tau and GG Tau and HD 283759 (but the latter is not a member of the association).

Even though our spectroscopic observations include a slew of other molecular transitions, we only discuss here the results for [O I] 63 μm and 145 μm , as well as [C II] 158 μm . Results on the o-H₂O line at 63.32 μm were presented in Riviere-Marichalar et al. (2012) while other transitions, typically detected in strong outflow sources and sometimes spatially resolved, were discussed in Podio et al. (2012) for a subset of our sample.

The [O I] 63 μm line, spatially and spectrally unresolved in most sources, is by far the strongest line in our sample and often the only line detected, especially for fainter sources. With a typical line sensitivity of $\sim 1 \times 10^{-17} \text{ W m}^{-2}$, we obtained $>3\sigma$ detections in 43 out of 75 targets; no Class III sources were detected. Marginal (2σ – 3σ level) detections are presented for another 10 sources. The [O I] 145 μm line is 10–25 times fainter than the [O I] 63 μm line and detected only in 17 sources. The detection rate for [C II] 158 μm line is even lower (10 targets) and detections are restricted to jet/outflow sources.

We found no correlation between [O I] 63 μm line intensity and disk mass, suggesting that the line is either optically thick or is not a valuable direct probe the mass of the overall gas reservoir. However, we found a tight correlation between the [O I] 63 μm line strength and the 63 μm continuum flux density for “disk-only” objects, i.e., sources with no or only weak outflow activity. Sources with clear evidence for outflow activity, on the other hand, can show line strengths that are as much as 20 times higher than disk-only sources, suggesting that the line emission is dominated by the jet. Some outflow sources (6 out of 24), however, follow the disk correlation and show little or no excess due to the outflow. Among disk sources, transitional disks also stand out, being fainter in [O I] than CTTSs by a factor of two to three for comparable continuum flux densities.

The tight correlation between [O I] line and 63 μm continuum emissions in the disk-only sample suggests that they originate from the same region of the disk. Simple disk models indicate that the most of the far-infrared continuum emission arise from the inner disk regions (within 5–50 AU at most, depending on the disk outer radius). Based on two-component isothermal graybody fits to the millimeter and far-infrared SEDs, we suggest that the [O I] 63 μm emission and the 63 μm continuum emission originate from the inner disk and/or lower surface layers where the gas and the dust is thermalized. This can also explain the weaker line emission of transition disks, since the dust in these systems is substantially cooler. The absence of dependence of both the [O I] 63 μm line and far-infrared continuum emission strength on binary separation for systems

wider than 10 AU further supports the co-spatiality of their emitting regions and the fact that they are limited to the innermost regions of the disk.

The observations presented in this paper provide a rich dataset to test thermo-chemical models which will provide a better understanding of the origin and strength of the [O I] 63 μ m line in protoplanetary disks.

This work made extensive use of the SIMBAD Database, operated at CDS, Strasbourg, France, and NASA's Astrophysics Data System Abstract Service. We thank Uma Gorti for stimulating discussions. We thank the referee for a very careful reading of the manuscript and for his/her constructive criticism. F. Ménard acknowledges financial support from the Milenium Nucleus P10-022-F, funded by the Chilean Government, and by the EU FP7-2011 programme, under Grant Agreement 284405.

REFERENCES

- Agra-Amboage, V., Dougados, C., Cabrit, S., Garcia, P. J. V., & Ferruit, P. 2009, *A&A*, **493**, 1029
- Andrews, S. M., Wilner, D. J., Espaillat, C., et al. 2011, *ApJ*, **732**, 42
- Andrews, S. M., & Williams, J. P. 2005, *ApJ*, **631**, 1134
- Andrews, S. M., & Williams, J. P. 2007, *ApJ*, **659**, 705
- Aresu, G., Kamp, I., Meijerink, R., et al. 2013, *A&A*, submitted
- Baldovin-Saveedra, C., Audard, M., Güdel, M., et al. 2011, *A&A*, **528**, A22
- Beck, T. L., & Simon, M. 2001, *AJ*, **122**, 413
- Beckwith, S. V. W., Sargent, A. I., Chini, R. S., & Güsten, R. 1990, *AJ*, **99**, 924
- Bertout, C., Robichon, N., & Arenou, F. 1999, *A&A*, **352**, 574
- Boden, A. F., Torres, G., Duchêne, G., et al. 2012, *ApJ*, **747**, 17
- Bouvier, J., Alencar, S. H. P., Bouletier, T., et al. 2007, *A&A*, **463**, 1017
- Bouvier, J., Chelli, A., Allain, S., et al. 1999, *A&A*, **349**, 619
- Bouvier, J., Grankin, K. N., Alencar, S. H. P., et al. 2003, *A&A*, **409**, 169
- Brown, J. M., Blake, G. A., Qi, C., et al. 2009, *ApJ*, **704**, 496
- Bührke, T., Brugel, E. W., & Mundt, R. 1986, *A&A*, **163**, 83
- Cabrit, S., Edwards, S., Strom, S. E., & Strom, K. M. 1990, *ApJ*, **354**, 687
- Calvet, N., Muzerolle, J., Briceño, C., et al. 2004, *AJ*, **128**, 1294
- Carr, J. S., & Najita, J. R. 2008, *Sci*, **319**, 1504
- Chakraborty, A., & Ge, J. 2004, *AJ*, **127**, 2898
- Cieza, L. A., Olofsson, J., Harvey, P. M., et al. 2013, *ApJ*, **762**, 100
- Cieza, L. A., Padgett, D. L., Allen, L. E., et al. 2009, *ApJL*, **696**, L84
- Cohen, M., & Kuhl, L. V. 1979, *ApJS*, **41**, 743
- Cox, A. W., Grady, C. A., Hammel, H. B., et al. 2013, *ApJ*, **762**, 40
- Creech-Eakman, M. J., Chiang, E. I., Joungh, R. M. K., Blake, G. A., & van Dishoeck, E. F. 2002, *A&A*, **385**, 546
- Dahm, S. E., & Lyke, J. E. 2011, *PASP*, **123**, 1383
- Dent, W. F. R., Thi, W.-F., Kamp, I., et al. 2013, *PASP*, **125**, 477
- Dougados, C., Cabrit, S., Lavalley, C., & Ménard, F. 2000, *A&A*, **357**, L61
- Duchêne, G. 2010, *ApJL*, **709**, L114
- Duchêne, G., Ghez, A. M., McCabe, C., & Weinberger, A. J. 2003, *ApJ*, **592**, 288
- Duchêne, G., McCabe, C., Ghez, A., & Macintosh, B. A. 2004, *ApJ*, **606**, 969
- Duchêne, G., McCabe, C., Pinte, C., et al. 2010, *ApJ*, **712**, 112
- Dutrey, A., Guilloteau, S., Duvert, G., et al. 1996, *A&A*, **309**, 493
- Dutrey, A., Guilloteau, S., Piéty, V., et al. 2008, *A&A*, **490**, L15
- Edwards, S., Cabrit, S., Strom, S. E., et al. 1987, *ApJ*, **321**, 473
- Edwards, S., Fischer, W., Hillenbrand, A., & Kwan, J. 2006, *ApJ*, **646**, 319
- Edwards, S., Fischer, W., Kwan, J., Hillenbrand, A., & Dupree, A. K. 2003, *ApJL*, **599**, L41
- Eisloffel, J., & Mundt, R. 1998, *AJ*, **115**, 1554
- Espaillat, C., Furlan, E., D'Alessio, P., et al. 2011, *ApJ*, **728**, 49
- Fischer, W., Edwards, S., Hillenbrand, L., & Kwan, J. 2011, *ApJ*, **730**, 73
- Flower, D. R., & Pineau des Fôrets, G. 2010, *MNRAS*, **406**, 1745
- Forrest, W. J., Sargent, B., Furlan, E., et al. 2004, *ApJS*, **154**, 443
- Furlan, E., Luhman, K. L., Espaillat, C., et al. 2011, *ApJS*, **195**, 1
- Glauser, A. M., Ménard, F., Pinte, C., et al. 2008, *A&A*, **485**, 531
- Gómez, M., Whitney, B. A., & Kenyon, S. J. 1997, *AJ*, **114**, 1138
- Gorti, U., & Hollenbach, D. 2008, *ApJ*, **683**, 287
- Gorti, U., Hollenbach, D., Najita, J., & Pascucci, I. 2011, *ApJ*, **735**, 90
- Guilloteau, S., Dutrey, A., Piéty, V., & Boehler, Y. 2011, *A&A*, **529**, A105
- Guilloteau, S., Dutrey, A., & Simon, M. 1999, *A&A*, **348**, 570
- Gullbring, E., Hartmann, L., Briceño, C., & Calvet, N. 1998, *ApJ*, **492**, 323
- Haisch, K. E., Lada, E. A., & Lada, C. J. 2001, *ApJL*, **553**, L153
- Harris, R. J., Andrews, S. M., Wilner, D. J., & Kraus, A. L. 2012, *ApJ*, **751**, 115
- Hartigan, P., Edwards, S., & Ghandour, L. 1995, *ApJ*, **452**, 736
- Hartmann, L. 2003, *ApJ*, **585**, 398
- Hartmann, L., Calvet, N., Watson, D. M., et al. 2005, *ApJL*, **628**, L147
- Hernández, J., Hartmann, L., Calvet, N., et al. 2008, *ApJ*, **686**, 1195
- Hirth, G. A., Mundt, R., & Solf, J. 1997, *A&AS*, **126**, 437
- Hirth, G. A., Mundt, R., Solf, J., & Ray, T. P. 1994, *ApJL*, **427**, L99
- Hollenbach, D., & McKee, C. F. 1989, *ApJ*, **342**, 306
- Horne, K. 1986, *PASP*, **98**, 609
- Ireland, M. J., & Kraus, A. L. 2008, *ApJL*, **678**, L59
- Isella, A., Carpenter, J. M., & Sargent, A. I. 2009, *ApJ*, **701**, 260
- Isella, A., Carpenter, J. M., & Sargent, A. I. 2010, *ApJ*, **714**, 1746
- Isobe, T., Feigelson, E. D., & Nelson, P. I. 1986, *ApJ*, **306**, 4909
- Kamp, I., Tilling, I., Woitke, P., Thi, W.-F., & Hogerheijde, M. 2010, *A&A*, **510**, A18
- Kamp, I., Woitke, P., Pinte, C., et al. 2011, *A&A*, **532**, A85
- Karska, A., Herczeg, G. J., van Dishoeck, E. F., et al. 2013, *A&A*, **552**, A141
- Kenyon, S. J., Brown, D. I., Tout, C. A., & Berlind, P. 1998, *AJ*, **115**, 2491
- Kenyon, S. J., Gómez, M., & Whitney, B. 2008, in *Handbook of Starforming Regions*, Vol. I, ed. B. Reipurth (San Francisco, CA: ASP), 405
- Kenyon, S. J., & Hartmann, L. 1995, *ApJS*, **101**, 117
- Kepner, J., Hartigan, P., Yang, C., & Strom, S. 1993, *ApJL*, **L119**
- Koresko, C. D. 2000, *ApJL*, **531**, L147
- Kraus, A. L., & Hillenbrand, L. A. 2009, *ApJ*, **703**, 1511
- Kraus, A. L., Ireland, M. J., Hillenbrand, L. A., & Martinache, C. 2012, *ApJ*, **745**, 19
- Kraus, A. L., Ireland, M. J., Martinache, F., & Hillenbrand, L. A. 2011, *ApJ*, **731**, 8
- Krist, J. E., Stapelfeldt, K. R., Golimowski, D. A., et al. 2005, *AJ*, **130**, 2778
- Küçük, İ., & Akkaya, İ. 2010, *RMxAA*, **46**, 109
- Kwan, J., & Fischer, W. 2011, *MNRAS*, **411**, 2383
- Lay, O. P., Carlstrom, J. E., & Hills, R. E. 1997, *ApJ*, **489**, 917
- Leinert, Ch., Haas, M., Richichi, A., Zinnecker, H., & Mundt, R. 1991, *A&A*, **250**, 407
- Liseau, R., Justtanont, K., & Tielens, A. G. G. M. 2006, *A&A*, **446**, 561
- Lommen, D. J. P., van Dishoeck, E. F., Wright, C. M., et al. 2010, *A&A*, **515**, A77
- Lorenzetti, D. 2005, *SSRv*, **119**, 181
- Luhman, K. L., Allen, P. R., Espaillat, C., Hartmann, L., & Calvet, N. 2010, *ApJS*, **186**, 111
- Markwardt, C. B. 2009, in *ASP Conf. Ser. 411, Astronomical Data Analysis Software and Systems XVIII*, ed. D. A. Bohlender, D. Durand, & P. Dowler (San Francisco, CA: ASP), 251
- Martín, E. L., Rebolo, R., Magazzù, A., & Pavlenko, Y. V. 1994, *A&A*, **282**, 503
- Massarotti, A., Latham, D. W., Torress, G., Brown, R. A., & Oppenheimer, B. D. 2005, *AJ*, **129**, 2294
- Massi, M., Ros, E., Menten, K. M., et al. 2008, *A&A*, **480**, 489
- McCabe, C., Duchêne, G., & Ghez, A. M. 2002, *ApJ*, **575**, 974
- McGroarty, F., & Ray, T. P. 2004, *A&A*, **420**, 975
- Meeus, G., Montesinos, B., Mendigutía, I., et al. 2012, *A&A*, **544**, A78
- Meijerink, R., Aresu, G., Kamp, I., et al. 2012, *A&A*, **547**, A68
- Meijerink, R., Glassgold, A. E., & Najita, J. R. 2008, *ApJ*, **676**, 518
- Mitchell, G. F., Sargent, A. I., & Mannings, V. 1997, *ApJL*, **483**, L127
- Monin, J.-L., & Bouvier, J. 2000, *A&A*, **356**, L75
- Mora, A., Merín, B., Solano, E., et al. 2001, *A&A*, **378**, 116
- Movsessian, T. A., Magakian, T. Y., Bally, J., et al. 2007, *A&A*, **470**, 605
- Müller, T., Nielbock, M., Balog, Z., Klaas, U., & Vilenius, E. 2011, *PACS Photometer: Point-Source Flux Calibration*, Technical Report PICC-ME-TN-037 (Germany: MPE)
- Mundt, R., Brugel, E. W., & Bührke, T. 1987, *ApJ*, **319**, 275
- Mundt, R., & Fried, J. W. 1983, *ApJL*, **274**, L83
- Mundt, R., Ray, T. P., Bührke, T., Raga, A. C., & Solf, J. 1990, *A&A*, **232**, 37
- Najita, J. R., Doppmann, G. W., Bitner, M. A., et al. 2009, *ApJ*, **697**, 957
- Najita, J. R., Strom, S. E., & Muzerolle, J. 2007, *MNRAS*, **378**, 369
- Nisini, B., Giannini, T., & Lorenzetti, D. 2002, *ApJ*, **574**, 246
- O'Neal, D., Feigelson, E. D., Mathieu, R. D., & Myers, P. C. 1990, *AJ*, **100**, 1610
- Osterloh, M., & Beckwith, S. V. W. 1995, *ApJ*, **439**, 288
- Ott, S. 2010, in *ASP Conf. Ser. 434, Astronomical Data Analysis Software and Systems XIX*, ed. Y. Mizumoto, K.-I. Morita, & M. Ohishi (San Francisco, CA: ASP), 139
- Piétu, V., Dutrey, A., Guilloteau, S., Chapillon, E., & Pety, J. 2006, *A&A*, **460**, L43
- Pinte, C., Ménard, F., Duchêne, G., & Bastien, P. 2006, *A&A*, **459**, 797
- Pinte, C., Woitke, P., Ménard, F., et al. 2010, *A&A*, **518**, L126

- Podio, L., Kamp, I., Codella, D., et al. 2013, [ApJL](#), **766**, L5
- Podio, L., Kamp, I., Flower, D., et al. 2012, [A&A](#), **545**, 44
- Poglitsch, A., Waelkens, C., Geis, N., et al. 2010, [A&A](#), **518**, L2
- Pilbratt, G. L., Riedinger, J. R., Passvogel, T., et al. 2010, [A&A](#), **518**, L1
- Rebull, L. M., Koenig, X. P., Padgett, D. L., et al. 2011, [ApJS](#), **196**, 4
- Rebull, L. M., Padgett, D. L., McCabe, C.-E., et al. 2010, [ApJS](#), **186**, 259
- Reipurth, B., Bally, J., & Devine, D. 1997, *AJ*, **114**, 270
- Ricci, L., Testi, L., Natta, A., et al. 2010, [A&A](#), **512**, A15
- Ricci, L., Trotta, F., Testi, L., et al. 2012, [A&A](#), **540**, A6
- Riviere-Marichalar, P., Ménard, F., Thi, W. F., et al. 2012, [A&A](#), **538**, L3
- Roddier, C., Roddier, F., Northcott, M. E., Graves, J. E., & Jim, K. 1996, [ApJ](#), **463**, 326
- Rodmann, J., Henning, Th., Chandler, C. J., Mundy, L. G., & Wilner, D. J. 2006, [A&A](#), **446**, 211
- Simon, M., & Guilloteau, S. 1992, [ApJL](#), **397**, L47
- Simon, M., Holfeltz, S. T., & Taff, L. G. 1996, [ApJ](#), **469**, 890
- Stapelfeldt, K. R., Ménard, F., Watson, A. M., et al. 2003, [ApJ](#), **589**, 410
- St-Onge, G., & Bastien, P. 2008, [ApJ](#), **674**, 1032
- Strom, K. M., Strom, S. E., Edwards, S., Cabrit, S., & Skrutskie, M. F. 1989, [AJ](#), **97**, 1451
- Sturm, B., Bouwman, J., Henning, Th., et al. 2010, [A&A](#), **518**, L129
- Terada, H., Tokunaga, A. T., Kobayashi, N., et al. 2007, [ApJ](#), **667**, 303
- Tielens, A. G. G. M., & Hollenbach, D. 1985, [ApJ](#), **291**, 722
- Torres, R., Loinard, L., Mioduszewski, A. J., & Rodríguez, L. F. 2009, [ApJ](#), **698**, 242
- Vandenbussche, B., Blommaert, J., Contursi, A., et al. 2011, PACS Spectroscopy Performance and Calibration, Technical Report PICC-KL-TN-041 (Germany: MPE)
- van Kempen, T. A., Kristensen, L. E., Herczeg, G. J., et al. 2010, [A&A](#), **518**, L121
- Welty, A. D. 1995, [AJ](#), **110**, 776
- White, R. J., & Ghez, A. M. 2001, [ApJ](#), **556**, 265
- White, R. J., Ghez, A. M., Reid, I. N., & Schultz, G. 1999, [ApJ](#), **520**, 811
- White, R. J., & Hillenbrand, L. A. 2004, [ApJ](#), **616**, 998
- White, R. J., & Hillenbrand, L. A. 2005, [ApJL](#), **621**, L65
- Woitak, J., & Leinert, Ch. 1998, [A&A](#), **338**, 122